3-22-2018

Plasmonic Grating Geometrics and Wavelength-dependent Focus Depth in Infrared Detectors

Patrick R. Kennedy

PLASMONIC GRATING GEOMETRIES AND WAVELENGTH-DEPENDENT FOCUS DEPTH IN INFRARED DETECTORS

THESIS

Patrick R. Kennedy, Capt, USAF

AFIT-ENG-MS-18-M-038

DEPARTMENT OF THE AIR FORCE
AIR UNIVERSITY

AIR FORCE INSTITUTE OF TECHNOLOGY

Wright-Patterson Air Force Base, Ohio

AFIT-ENG-MS-18-M-038

PLASMONIC GRATING GEOMETRIES AND WAVELENGTH-DEPENDENT FOCUS DEPTH IN INFRARED DETECTORS

THESIS

Presented to the Faculty

Department of Electrical and Computer Engineering

Graduate School of Engineering and Management

Air Force Institute of Technology

Air University

Air Education and Training Command

in Partial Fulfillment of the Requirements for the

Degree of Masters of Science in Electrical Engineering

Patrick R. Kennedy, B.S.E.E

Capt, USAF

22 March 2018

AFIT-ENG-MS-18-M-038

PLASMONIC GRATING GEOMETRIES AND WAVELENGTH-DEPENDENT FOCUS DEPTH IN INFRARED DETECTORS

THESIS

Patrick R. Kennedy, B.S.E.E
Capt, USAF

Committee Membership:

Maj Tod Laurvick, Ph.D.
Chairman

Capt Robert A. Lake, Ph.D.
Member

Danhong Huang Ph.D.
Member

AFIT-ENG-MS-18-M-038

Abstract

The objective for this research is to determine a relationship between plasmonic grating geometries and the wavelength-dependent focus depth. This research is focused on enhancing the signal collected by infrared detectors by using a metal grating as a planar lens to focus light in the detecting region of the substrate. This can be used to maintain a thinner absorbing region and possibly to create multi-color imaging in a single pixel. Simulations demonstrate that the plasmonic lens is capable of creating a wavelength dependent focus spot.

Acknowledgements

I would like to thank Maj Tod Laurvick for keeping me on track. Thank you to AFRL/RV for funding this research.

Patrick R. Kennedy

Table of Contents

Page

List of Figures

Figure Page

Figure Page

List of Tables

List of Abbreviations

Abbreviation		Page
IR	Infrared	1
LWIR	long wave infrared	2
MWIR	mid wave infrared	3
FDFD	finite difference frequency domain	5
SPP	surface plasmon polaritons	5
FDTD	finite difference time domain	7
TE	transverse electric	13
TM	transverse magnetic	13

PLASMONIC GRATING GEOMETRIES AND WAVELENGTH-DEPENDENT FOCUS DEPTH IN INFRARED DETECTORS

I. Introduction

Infrared (IR) detectors are used in variety of military and civilian applications. Users are always looking to be able to detect dimmer and more distant targets. In order to increase the number of targets to be effective in these applications, the detector should have a high quantum efficiency and low signal to noise ratio. Quantum efficiency is defined as the fraction of photons converted to electrical current. The quantum efficiency of these detectors has traditionally been increased by increasing the width of the absorbing region. The cost is increased dark current which reduces the signal to noise ratio. Dark current acts as noise floor because it is the current which flows while their is no illumination present on the detector.

1.1 Infrared Detectors

An infrared photodetector senses incoming infrared light by absorbing the incoming photons and converting them into electrical current. This is done when the photon creates and electron-hole pair in a semiconductor material where the newly created charge carriers can be swept out of the absorption region by the electric field which is present within. This is made possible by the conduction and valance band structures present in semiconductors [1].

A semiconductor is a material where the conduction band and valance band of electrons are separated by a gap which is sufficiently large that electrons can't transition from one band to the other without the addition of energy. Semiconductors

used for photodetection must have a bandgap smaller in energy than the photons to be detected. For this reason, photons in the long wave infrared region require semiconductors with smaller bandgaps than traditional semiconductors. Infrared photons can have energies ranging from 1.24 meV to 1.7 eV. For long wave infrared (LWIR), the photon energies can be from roughly 80-150 meV. Since typical optical semiconductors such as Si, Ge, and GaAs all have larger bandgaps, other materials must be used. The dominant material for infrared photodetection since the late 70's has been HgCdTe [2]. This is a homogenous material where the ratio of Hg to Cd determines the bandgap [3]. InSb and InGaAs have also been used in the same manner. An alternative to the traditional photodetector is the GaAs/AlGaAs quantum well superlattices. In these devices the transition takes place in the quantum well formed by the conduction bands of the two materials. The advantage to these devices is that GaAs is already widely used, but they suffer from performance issues such as low quantum efficiencies. A third device is the broken gap strained layer superlattices. These devices use materials with offset bandgaps such that the conduction band of one is lower than the valance band edge of the other. The bandgap can then be tuned by the widths of the individual layers. This type of device has a number of issues such as the relatively short carrier lifetimes [2].

Any improvement in the capability of infrared detectors is a benefit the military. Due to Plank's Law, hot objects radiate mostly in the infrared. Plank's law dictates that black bodies will emit radiation with a distribution that is a function of temperature. When an object heats up, the wavelength of peak power decreases. There is always a demand for the ability to detect cooler objects which requires higher sensitivity and the ability to detect longer wavelengths.

The wavelengths of interest are largely influenced by atmospheric windows. The molecules in the atmosphere absorb infrared in specific wavelengths. The regions of

the spectrum where the radiation is not absorbed are called windows. There is a window in the 3-4 micron range and one in the 8-14 micron range. These two regions are commonly referred to as mid wave infrared (MWIR) and LWIR.

Infrared detection can be classified by photon detectors and thermal detectors. Thermal detectors detect a wide band of frequencies due to the thermal effect that all IR radiation provided. Photon detectors allow more specific detection based on the band structure of the semiconductor, as discussed above.

1.2 Plasmonics

A possible solution to counter the drawbacks of infrared detectors is to find a way to confine the light to a thinner absorbing layer. A plasmonic grating lens has been shown to be able to focus incident light to a smaller area of the substrate. [4] [5]

Also, users often want the ability to detect multiple regions of the IR spectrum at the same time. The plasmonic gratings can enable this by focusing light of different wavelengths at different depths in the substrate. Devices would then be built with detectors at the appropriate depths below the grating. This will create added benefit toward reducing the size, cost, and complexity of the the total system.

Current work shows that that plasmonic gratings are able to act as planar lenses with a focusing at a particular depth in the device. This work will characterize the wavelength dependence of focus depth with these gratings. Current research focuses on monochromatic detection, usually a wavelength corresponding to a laser source the researcher has in their lab. For this work, I will use wavelengths at many frequencies across the infrared spectrum.

II. Literature Review

2.1 Improving Infrared Photodetectors using Plasmonic Lenses

Since the objective of the research is to enhance infrared photodetectors, this chapter will start with a short review of those detectors. Next, literature closely related to plasmonic lenses will be looked at. This will be followed up by a review of plasmonics. Finally, there will be an overview of the simulation method to be used.

2.2 Infrared Detectors

One newer type of photon infrared detector is the type-II InAs/GaSb superlattice detector. Type-II superlattices are heterostructures where the conduction band edge of one material is of a lower energy than the valance band edge of the second material. This sort of structure has been formed by InAs/GaSb or InGaAs/GaSbAs. In this case, the valence band edge of GaSb is 0.14 eV higher than the conduction band edge of InAs. This is called the broken-gap band alignment. This superlattice structure has been proposed for use in infrared photodetectors to replace the currently used HgCdTe infrared photodetectors. In these photodetectors, bandgap is inversely proportional to layer thickness. This means layers must be relatively thick for LWIR detection. Additionally, since absorption occurs at the interfaces, the strength of absorption is proportional to the number of interfaces. These two factors present a challenge for creating detectors with small band gaps. This has been addressed with an InAs/GaInSb strained layer superlattice which places the InAs under tension and the GaInSb under compression. This has the impact of adjusting band edges in each material which allows for thinner layers [6] [7].

2.3 Related Research

The literature included examples of nanoscale metal geometries being used to create planar lenses using plasmonics. One major paper which inspired this research was *Planar Lenses Based on Nanoscale Slit Arrays in a Metallic Film.* In this paper, researchers used ion beam milling to etch linear slits into a metal film over a fused silica substrate. The experiment was performed by illuminating the grating with a 637nm laser which was large enough to be considered a plane wave source on the device. The region below the laser was measured using a confocal microscope to chart the response. Additionally, the authors performed a finite difference frequency domain (FDFD) simulation to determine if this would yield the same results. The researchers found strong agreement between the experimental data and the simulation results. They found that depth of maximum intensity, or the focal length of the lens was largely determined by the size of the lens[5].

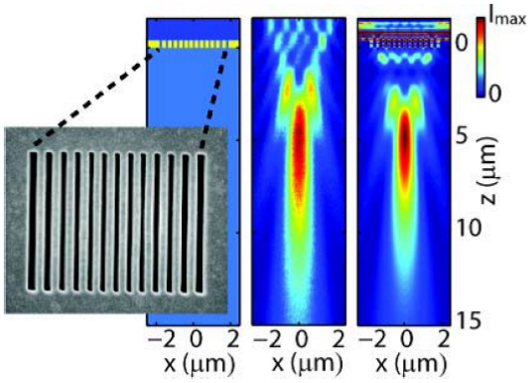

Figure 1. Results from experiment performed by at Stanford

In the same year, researchers at Air Force Research Lab published a paper describing the physics of a grating built with grooves on both sides of the metal film. The paper provides a Green's function formalism to describe the interaction of surface plasmon polaritons (SPP) with an air, metal, substrate interface. They studied effects of depth ratio, groove separation, and lattice constant on transmissivity and found

peaks in the transmissivity corresponding to features in the metal film[8]. A similar paper, published in 2010, further illustrated how plasmonic gratings bend light. The paper *Beam bending via plasmonic lenses* explored three types of asymmetric lens design to show how it would bend light[9]. The results are in reasonable agreement with the work from Stanford in Planar Lenses Based on Nanoscale Slit Arrays in a Metallic Film. These papers were preceded by Focal length modulation based on a metallic slit surrounded with grooves in curved depths where Shi numerically characterized the focal position through a plasmonic lens[10]. The foundational paper to inspire much of the work by Ebbesen *et al.* investigated transmission through two dimensional hole arrays and found transmission peaks at certain wavelengths depending on the thickness and geometry of the silver film[11]. Later, plasmonic lenses using dot arrays were shown to be able to create a variety of focal patterns below the lens[12] In most of these applications visible light is used as the source. The permittivities of gold and silver in the visible spectrum are well described by the Lorentz-Drude model for dispersive media, which will be discussed in more depth later[13] [14].

2.4 Plasmonic Fundamentals

Broadly speaking, plasmons are oscillations of electrons in a metal or semiconductor. A wide variety of geometries can be used to take advantage of coupling of optical waves to these electron oscillations for various applications in sensing and waveguiding. Gold, silver, and copper are most commonly associated with the field of plasmonics because of their utility in the visible spectrum. More specifically, surface plasmons are plasmons which propagate along metal-dielectric interfaces[15]. The nature of these surface plasmons is rooted in quantum mechanics, but the effects can be well described by classical electrodynamics. One method commonly used to model a variety of plasmonic systems is Finite Difference Time Domain (FDTD)[15]. This

simulation technique is executed by solving Maxwell's curl equations in discreet time steps. The simulation domain is an offset grid to solve the electric and magnetic fields in alternating time steps. This can be done using a one, two or three dimensional grid [16]. The work of Baumeier *et al.* sought to calculate transmission of p- and s-polarized light through thin metal films. It was noted that transmission can occur even when slits or grooves dont pierce the film. The transmission is a result of the SPPs located at the dielectric interface. This effect worked for surfaces with periodic corrugations. It was found that for periodically corrugated surfaces, transmission was enhanced for both p- and s-polarized light[17].

2.5 FDTD and the Lorentz-Drude Model

In order for finite difference time domain (FDTD) simulations to accurately model the plasmonic response, the software must have the correct real and imaginary permittivity for whichever material is being modeled. For gold, the real and imaginary values for permittivity vary greatly at various frequencies or wavelengths[14]. The complex relative permativity can be written as

$$\varepsilon_r(\omega) = \varepsilon_r^f(\omega) + \varepsilon_r^b(\omega) \tag{1}$$

where $\varepsilon_r^f(\omega)$ describes the Drude model and $\varepsilon_r^b(\omega)$ describes the Lorentz model. The Drude Model is expressed as

$$\varepsilon_r^f(\omega) = 1 - \frac{\Omega_p^2}{\omega(\omega - j\Gamma_0)} \tag{2}$$

and the Lorentz Model is expressed as

$$\varepsilon_r^b(\omega) = \sum_{i=1}^{k} \frac{f_i \omega_p^2}{(\omega_i^2 - \omega^2) + j\omega\Gamma_i} \tag{3}$$

where ω_p is the plasma frequency, k is the number of oscillators with frequency ω_i, strength f_i, lifetime $1/\Gamma_i$ and $\Omega_p = \sqrt{f_o \omega_p}$ [14][13].

2.6 Summary

It has been shown that FDTD is sufficient to simulate plasmonic effects. This allows various designs to be explored moving forward. From there, more informed design decisions can be made when building real devices suitable for both dim-object detection and multispectral detection.

III. Methodology

3.1 Objective

The overarching goal of this research thread is to determine what plasmonic grating designs, if any, will improve the detection capabilities of photo detectors. In future research simulated results will be compared to devices built in a lab. Toward this effort, simulations will be used to show a relationship between lens characteristics and focal depth as well as intensity. The first step was to model devices already in literature to validate that the software would provide reliable results. The next step was to identify what characteristics of the lenses would be investigated. Those features would be modified and simulated to provide a full picture of how to design a plasmonic lens.

3.2 Software Evaluation

The first part of the research was to duplicate previous work to validate that simulation settings could be used to reliably predict performance of each lens. The simulation method used is called finite difference time domain (FDTD). FDTD simulated electromagnetic fields and waves by solving Maxwell's equations in discrete time steps using a rectangular mesh. During each half time step, the electric field is calculated from the magnetic field or vice-versa [16].

Two software packages were explored for the simulations: Sentaurus EMW by Synopsys and OptiFDTD by Optiwave. The original plan was to use both simulation packages to validate results, and choose the software best suited for the research. Both software packages were reviewed to determine which would be better suited for this research. Sentaurus EMW was found to return results consistent with previous work.

When performing an FDTD simulation, there are multiple considerations that can influence the accuracy of the result. In the spatial domain, mesh size must be small enough to accurately define the device, but smaller mesh cells come at the price of longer simulation times and higher memory requirements. Additionally, at the beginning of this research, the intent was to perform simulations in 3D for additional design possibilities. Due to the increase in simulation time for 3D simulations, as well as the fact that the gratings used are uniform in the z direction, 2D simulations were used for the experiment. Another parameter which effect accuracy is the time step. Sentaurus EMW automatically chooses an appropriate time step based on mesh size source frequency. Optiwave offers a time step, but allows you to change it.

In order for the software to correctly simulate the plasmonic behavior of gold, the Lorentz-Drude model for dispersive media must be used. The model has a variable complex refractive index depending on wavelength. In order for the simulation to be valid, the model must be valid for the chosen wavelength. The Sentaurus software package comes with a model that is valid for 300nm to 1000 nm. In order to explore longer wavelengths, additional data for the model will need to be provided.

3.2.1 OptiFDTD Procedure.

Optiwave OptiFDTD is broken into two parts: Designer, and Analyzer. Designer is where the materials, components, and sources are defined. The user places detectors which record the results and defines simulation parameters. Once the simulation has been run, the results are viewed in Analyzer.

The first step in setting up a simulation is to define the materials present. OptiFDTD uses a profile designer window to make these additions. Figure 2 shows the provided Lorentz-Drude model for gold in the OptiFDTD package.

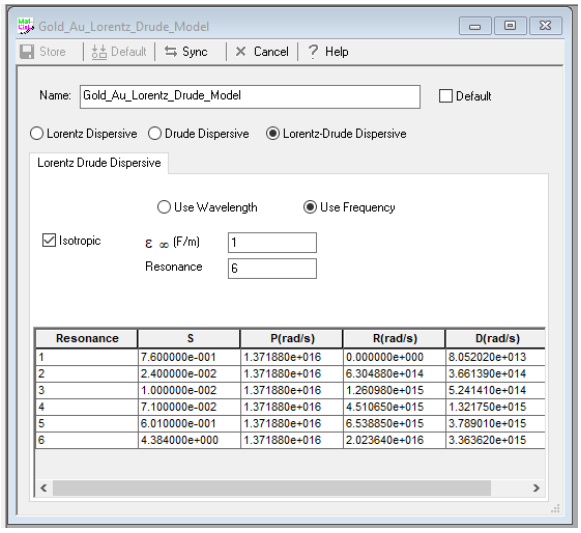

Resonance	S	P(rad/s)	R(rad/s)	D(rad/s)
1	7.600000e-001	1.371880e+016	0.000000e+000	8.052020e+013
2	2.400000e-002	1.371880e+016	6.304880e+014	3.661390e+014
3	1.000000e-002	1.371880e+016	1.260980e+015	5.241410e+014
4	7.100000e-002	1.371880e+016	4.510650e+015	1.321750e+015
5	6.010000e-001	1.371880e+016	6.538850e+015	3.789010e+015
6	4.384000e+000	1.371880e+016	2.023640e+016	3.363620e+015

Figure 2. Window for defining material parameters in OptiFDTD

Next, in the Designer window the user must create add components using the materials specified. To verify the suitability of this software for testing plasmonic gratings, the design used Verslegers *et al.* was duplicated. Both 2D and 3D devices were tested, as the software supports either. Figure 3 shows a window with components in place. Each block is a gold piece to make up the grating. This figure also shows two observation areas and the input plane.

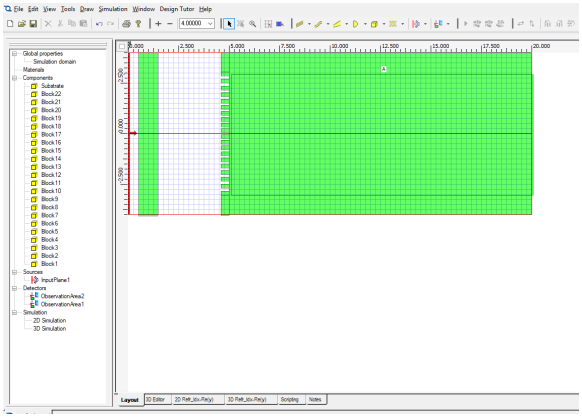

Figure 3. Window for building devices in OptiFDTD

An observation area is placed behind the lens to detect the response and another observation area was placed in front of the lens to verify the input signal was being

produced as intended. The input plane on the far left is used to create the input signal. Clicking InputPlane1 opens Input Field Properties which houses all the settings for the input signal including wavelength, amplitude, polarization, and other settings.

The bottom of the sidebar in Figure 3 shows 2D Simulation and 3D Simulation. Clicking either opens the settings for each including the option to run a simulation. This is where mesh size, time step size, total number of time steps, and boundary conditions are specified. Once the simulation is complete, the results can be viewed in OptiFDTD Analyzer. The Analyzer offers windows for electric field, magnetic field, and Poynting vector in the X, Y, and Z directions.

3.2.2 Sentaurus Procedure.

The Sentaurus software package is separated into multiple modules that have the ability to work off each others results. The individual software pieces being used are Device Editor, Mesh, EMW, and Visual. The Device Editor features a GUI where the device is built. Additionally, every action taken in the editor can be represented by a scripting command, allowing for multiple devices to be created with a single script. The final script used to create devices is in Appendix A. The device editor outputs a boundary file describing the device for the rest of the Sentaurus package.

The next step is to build the mesh using Sentaurus Mesh. Mesh receives the boundary file as an input along with a command file describing settings such as wavelength and creates a suitable mesh. Mesh cell sizes were bounded to between 0.001 microns and 0.05 microns.

Once the mesh is created, Sentaurus EMW takes the mesh file as input to begin the simulation. A command file was used define simulation parameters. Total time steps was set to 200,000. If convergence was achieve prior to that, the simulation ended on convergence. The tolerance for convergence was set to $1 * 10^{-4} W/cm^2$.

Material models were also specified in the command file. Of particular importance, Gold was set to a user defined Lorentz-Drude model. The software is prepackaged with parameters for the Lorentz-Drude model in the visible spectrum. The boundary condition was set as a variable so each type of boundary could be tested.

The plane wave excitation is used to create the signal. A box is defined from which the signal is emitted. The variables theta, phi, and psi define the direction the signal travels and the polarization. Initially, both transverse electric (TE) and transverse magnetic (TM) were tested. The polarization resulting in the highest transmission (TE) was used for the full experiment. Wavelength was set as a variable, so multispectral performance could be tested. Intensity was set to $0.1 W/cm^2$. The number of signals to full power was set to 1 allowing the signal to turn on immediately.

The results of the simulation are then viewed in Sentaurus Visual. Visual can also be used to export results as images or .csv files. The tcl script used to export results is in Appendix A.

These four modules, along with others, are packaged together in Sentaurus Workbench. Through Workbench, full factorial experiments can be constructed with variables in the command files.

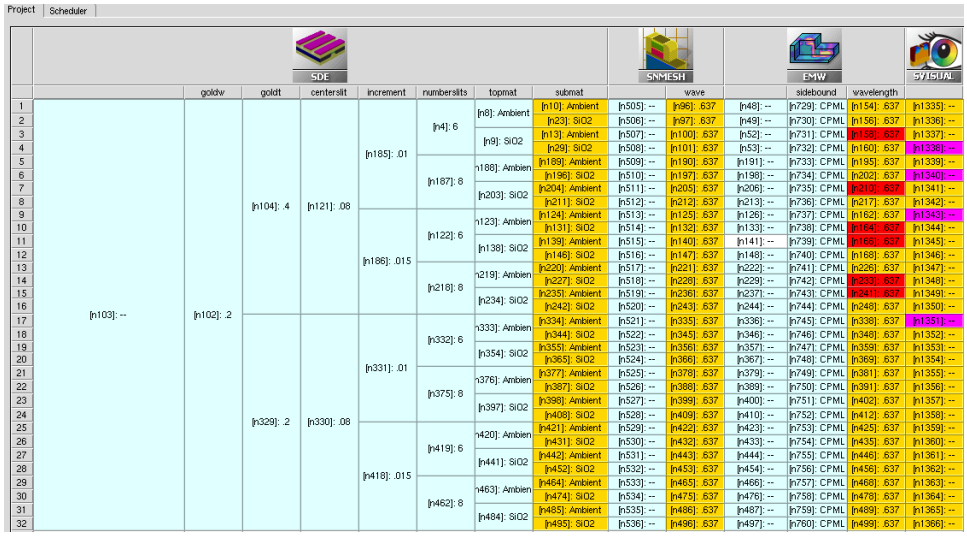

Figure 4. Table of settings in Sentaurus Workbench

3.3 Design of Experiments

For each plasmonic lens, five geometrical parameters have been identified as potential parameters of interest:

- thickness of the gold layer
- distance between each slit in the gold
- width of the center slit
- the rate at which slits grow wider on the outside of the lens
- the number of total slits

Additionally, the materials above and below the lens can be altered. For the duplication of the Stanford experiment, SiO_2 is used as the top material and air is below. For further experimentation, semiconductor substrate materials were tested.

The parameters investigated were gold thickness, rate of slit size change, and total number of slits. Width of gold in between slits and width of the center slit were held constant. Additionally, the material above and below the lens was chosed to be either air or SiO_2. Finally, two wavelengths were tested to determine multispectral performance.

Due to the choice to perform 2D experiments, a full factorial experiment was performed. The results include focus depth and intensity at focus. Each parameter was analyzed to determine its impact on each result. Recommendations follow from the analysis.

IV. Results

4.1 Software Evaluation

4.1.1 OptiFDTD.

This software never output results matching what was presented in the literature. Figure 5 shows the best results achieved through OptiFDTD while attempting to duplicate the experiment performed at Stanford. The results are not close enough to be useful, so this software was not used for any other simulations.

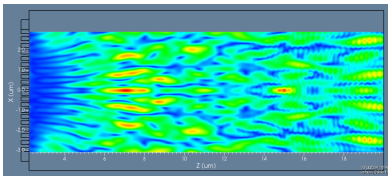

Figure 5. Heatmap of intensity while attempting to duplicate literature

4.1.2 Sentaurus EMW.

Sentaurus EMW did output a result close to matching previous work, validating its usefulness for the experiment. Figure 6 shows the results for the same design that was used by Verslegers *et al.*.

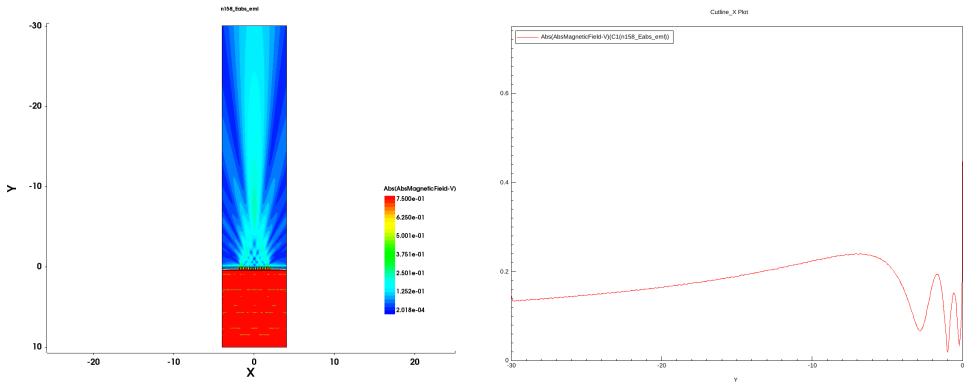

Figure 6. Results for lens designed to match Stanford lens

Sentaurus was also the best suited for running an experiment with multiple parameters. The program is built around scripting, making it suited for running multiple simulations in succession.

4.2 Design of Experiments Results

Figure 6 shows a somewhat ideal result for this experiment. Most of the energy is focused at a single focal point. The peak at 6.8 microns deep is clearly the focal point. While most results were straightforward, in some cases the far peak from the lens was lower than closer peaks as part of the triangle pattern that forms below the lens. Figure 7 shows one example. In these cases the largest peak not up against the lens was considered to be the focus depth as the far peak was much smaller and less useful.

The complete results are displayed in four tables with 16 trials in each table. The results were broken up into four tables for easier viewing. Each result for 637 nm is pictured in Appendix B and each result for 800 nm is pictured in Appendix C.

Table 1 includes all factors along with the intensity and focus depth results. It can be seen that focus depths range from roughly 1 micron to 21 microns proving a

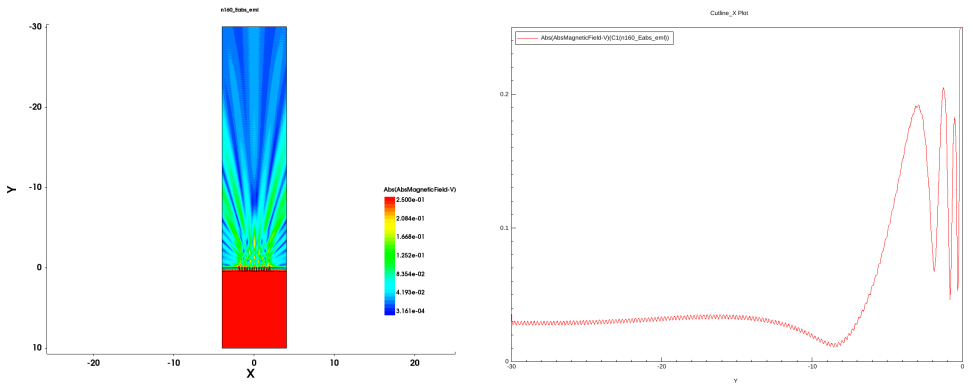

Figure 7. Results for 400nm gold thickness, 10nm increment,and 13 slits with SiO_2 top and SiO_2 bottom

large range. Intensities also vary by up to an order of magnitude. These results alone provide a decent basis for lens design impacting intensity and focus depth.

Table 1. Table of results for wavelength = 637 nm and gold thickness = 400nm

Thickness	Increment	Slits	Top	Substrate	Wavelength	Max Intensity	Focus Depth
0.4	0.01	13	Air	Air	0.637	0.5657	7.45
0.4	0.01	13	Air	SiO2	0.637	0.3232	12.1
0.4	0.01	13	SiO2	Air	0.637	0.2407	6.8
0.4	0.01	13	SiO2	SiO2	0.637	0.2053	1.3
0.4	0.01	17	Air	Air	0.637	0.6908	12.2
0.4	0.01	17	Air	SiO2	0.637	0.4127	20.8
0.4	0.01	17	SiO2	Air	0.637	0.2911	3.2
0.4	0.01	17	SiO2	SiO2	0.637	0.155	2.9
0.4	0.015	13	Air	Air	0.637	1.0727	7.1
0.4	0.015	13	Air	SiO2	0.637	0.4432	3.05
0.4	0.015	13	SiO2	Air	0.637	0.3251	7.75
0.4	0.015	13	SiO2	SiO2	0.637	0.4158	3.15
0.4	0.015	17	Air	Air	0.637	1.3722	11.55
0.4	0.015	17	Air	SiO2	0.637	0.6217	21.45
0.4	0.015	17	SiO2	Air	0.637	0.4047	13.75
0.4	0.015	17	SiO2	SiO2	0.637	0.3952	3.15

The results in Table 2 are similar to those in Table 1 but the gold layer was half as thick. Many of the results are similar, hinting that gold thickness is insignificant. Some discrepancies exist, but that could be a result of the different types of results described above.

Table 2. Table of results for wavelength = 637 nm and gold thickness = 200nm

Thickness	Increment	Slits	Top	Substrate	Wavelength	Max Intensity	Focus Depth
0.2	0.01	13	Air	Air	0.637	0.5133	1.6
0.2	0.01	13	Air	SiO2	0.637	0.33	11.65
0.2	0.01	13	SiO2	Air	0.637	0.3055	1.75
0.2	0.01	13	SiO2	SiO2	0.637	0.2849	0.6
0.2	0.01	17	Air	Air	0.637	0.5992	1.45
0.2	0.01	17	Air	SiO2	0.637	0.4069	20.15
0.2	0.01	17	SiO2	Air	0.637	0.4474	1.5
0.2	0.01	17	SiO2	SiO2	0.637	0.2722	2.7
0.2	0.015	13	Air	Air	0.637	0.7276	7.75
0.2	0.015	13	Air	SiO2	0.637	0.3745	13.9
0.2	0.015	13	SiO2	Air	0.637	0.6282	6.8
0.2	0.015	13	SiO2	SiO2	0.637	0.4918	1.4
0.2	0.015	17	Air	Air	0.637	0.925	12.8
0.2	0.015	17	Air	SiO2	0.637	0.5543	22.1
0.2	0.015	17	SiO2	Air	0.637	0.7254	13.45
0.2	0.015	17	SiO2	SiO2	0.637	0.5123	1.15

The results in Table 3 are otherwise identical to the results in Table 1 but were modeled from a longer wavelength. It should be noted that two simulations failed to provide convergent results. These entries were thrown out in the analysis. It is immediately obvious that intensity values are larger across the board. There also seems to be variation in focus depth which moves in both directions. Further analysis will be needed to draw deeper insight.

Table 3. Table of results for wavelength = 800 nm and gold thickness = 400nm

Thickness	Increment	Slits	Top	Substrate	Wavelength	Max Intensity	Focus Depth
0.4	0.01	13	Air	Air	0.8	1.978	6.15
0.4	0.01	13	Air	SiO2	0.8	2.0125	8.95
0.4	0.01	13	SiO2	Air	0.8	3.001	5.8
0.4	0.01	13	SiO2	SiO2	0.8	Failed	Failed
0.4	0.01	17	Air	Air	0.8	2.1893	10.5
0.4	0.01	17	Air	SiO2	0.8	2.204	14.95
0.4	0.01	17	SiO2	Air	0.8	3.2687	10.5
0.4	0.01	17	SiO2	SiO2	0.8	Failed	Failed
0.4	0.015	13	Air	Air	0.8	2.2649	6.55
0.4	0.015	13	Air	SiO2	0.8	2.266	9.5
0.4	0.015	13	SiO2	Air	0.8	3.1314	6.15
0.4	0.015	13	SiO2	SiO2	0.8	3.5095	8.9
0.4	0.015	17	Air	Air	0.8	2.497	11.3
0.4	0.015	17	Air	SiO2	0.8	2.5015	15.5
0.4	0.015	17	SiO2	Air	0.8	3.3195	10.95
0.4	0.015	17	SiO2	SiO2	0.8	3.8757	14.9

The results in Table 4 are from simulations using the 200nm gold layer with the 800nm wavelength. This time all simulations presented a solution. Intensity values remain high. Similar to the results in Table 2, focus depths will need analysis to draw proper conclusions. All successful trials will be included to build a linear regression model describing how each factor impacts the final results.

Table 4. Table of results for wavelength = 800 nm and gold thickness = 200nm

Thickness	Increment	Slits	Top	Substrate	Wavelength	Max Intensity	Focus Depth
0.2	0.01	13	Air	Air	0.8	2.5078	6.55
0.2	0.01	13	Air	SiO2	0.8	3.5095	9.5
0.2	0.01	13	SiO2	Air	0.8	2.2021	6.5
0.2	0.01	13	SiO2	SiO2	0.8	1.9312	9.15
0.2	0.01	17	Air	Air	0.8	2.7588	10.95
0.2	0.01	17	Air	SiO2	0.8	3.8135	15.5
0.2	0.01	17	SiO2	Air	0.8	2.4796	10.95
0.2	0.01	17	SiO2	SiO2	0.8	2.1622	15.45
0.2	0.015	13	Air	Air	0.8	2.6486	6.95
0.2	0.015	13	Air	SiO2	0.8	3.7069	10.05
0.2	0.015	13	SiO2	Air	0.8	2.5734	6.6
0.2	0.015	13	SiO2	SiO2	0.8	2.2769	9.7
0.2	0.015	17	Air	Air	0.8	2.8652	12.1
0.2	0.015	17	Air	SiO2	0.8	3.9399	16.6
0.2	0.015	17	SiO2	Air	0.8	2.9189	11.3
0.2	0.015	17	SiO2	SiO2	0.8	2.6157	16

V. Conclusions

5.1 Software Conclusions

Because FDTD simulations are a well defined method of solving Maxwell's equations in a stepwise manner, any FDTD software should yield accurate results assuming all materials were characterized correctly. In this case Sentaurus was best suited for the job, as it yielded results in reasonable agreement to previous work. Sentaurus also facilitated a large experiment with multiple factors. For this work, OptiFDTD never returned results matching what was expected. OptiFDTD is a software package primarily designed to analyze waveguides, so the interface was not designed with this application in mind.

5.2 Experiment Conclusions

A least squares fit model was used to analyze the effects of each parameter on focus depth and intensity at focus. JMP Pro was used to calculate the best fit using linear regression modeling.

The following plots show each parameter's impact on focus depth and intensity. The purpose of linear regression modeling is to prove or disprove the null hypothesis. That is the assertion that a given factor has no influence on the studied effect. For example, in Figure 10 the null hypothesis is the assertion that the increment parameter does not influence the maximum intensity at the focus spot. In this case the P value is 0.0085 indicating that the null hypothesis has a 0.85 percent chance of being true. Alternatively, that means there is a 99.15 percent chance that increment does influence the maximum intensity. From this we can conclude that increment should be considered in the design of future plasmonic lenses.

Figure 8 demonstrate the actual measured values compared to the predicted values based on the single factor model. The red line represents a perfect model.

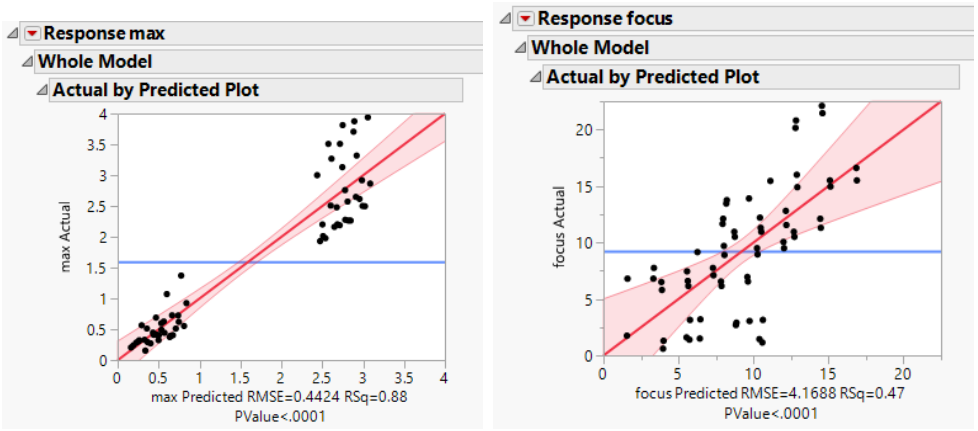

Figure 8. Whole model JMP output

Figure 9 show leverage plots for the thickness factor. In both cases it can be seen that thickness was not a significant factor in either result.

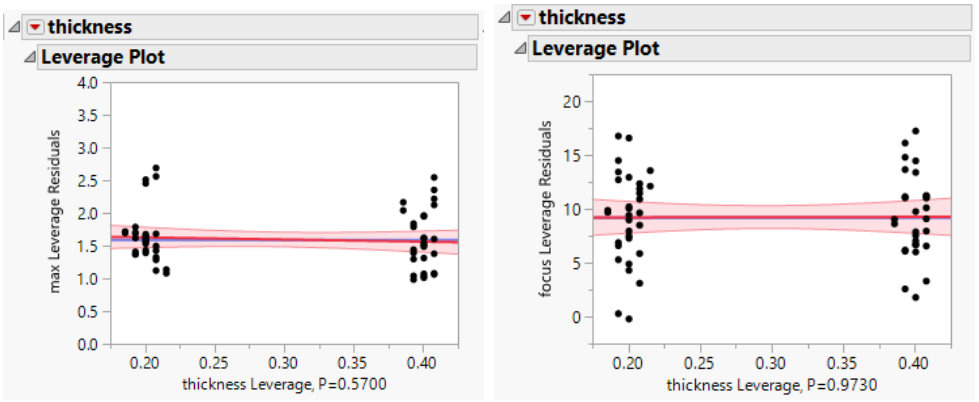

Figure 9. JMP output based on thickness

Figure 10 shows that the increment factor was found to have a significant impact on the maximum intensity. Also, the increment factor likely has an impact on the focus point, but more data would increase the certainty.

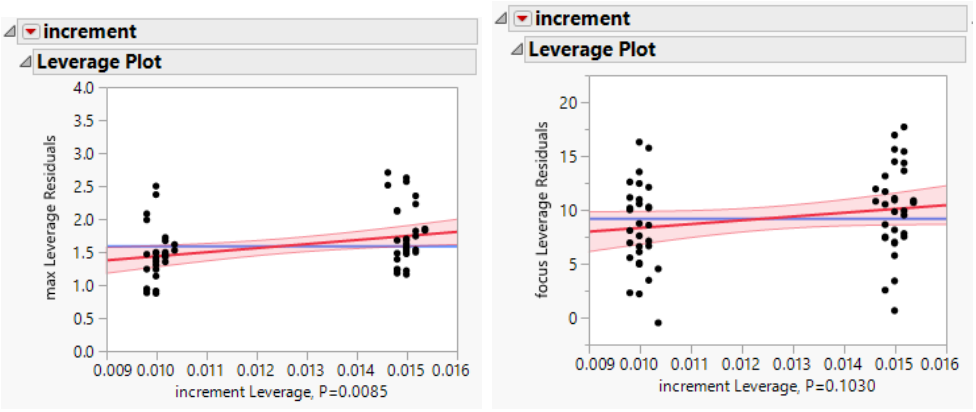

Figure 10. JMP output based on increment

Figure 11 confirms findings in previous work indicating that adding slits to the outside of the grating will change the focus depth. Also, Figure 11 shows that the number of slits likely influences the maximum intensity.

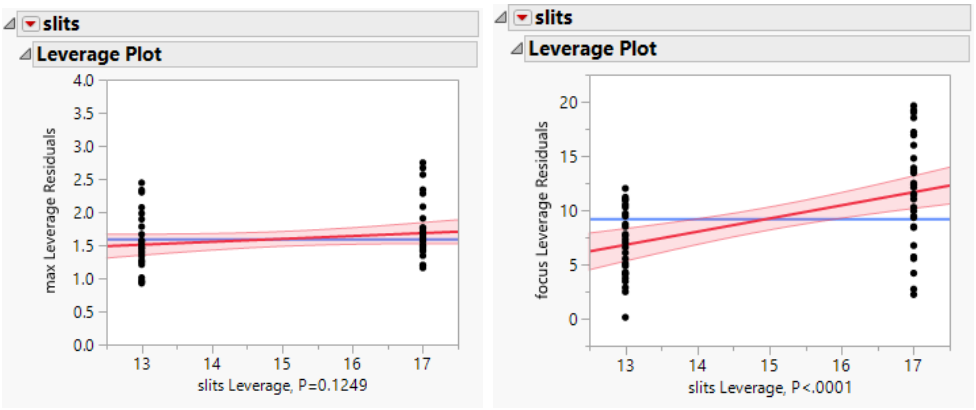

Figure 11. JMP output based on number of slits

Figures 12 and 13 show the leverage plots for the material above and below the grating. Intuitively material selection matters for focus depth. This would be seen with traditional lenses as well. Material choices did not impact max intensity in this case, but an non-transparent substrate may change this.

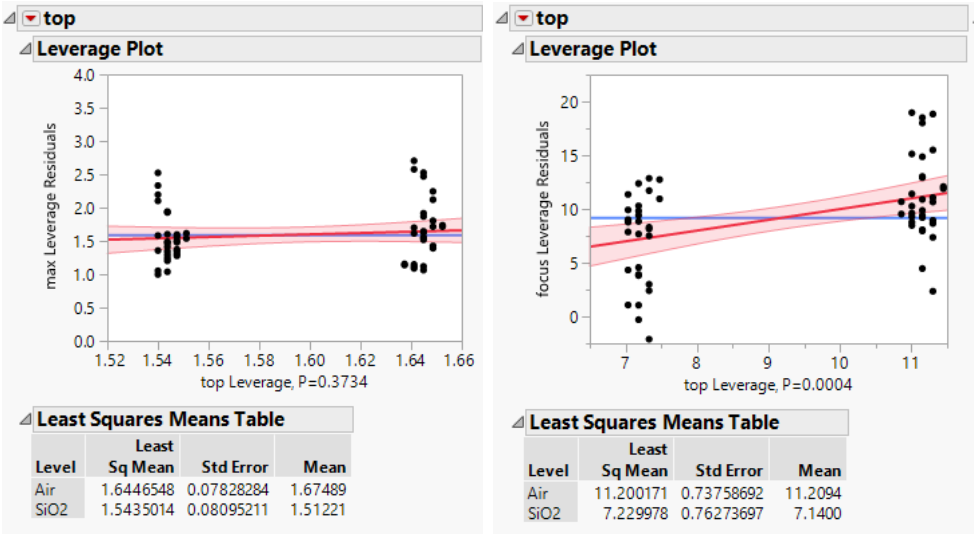

Figure 12. JMP output based on top material

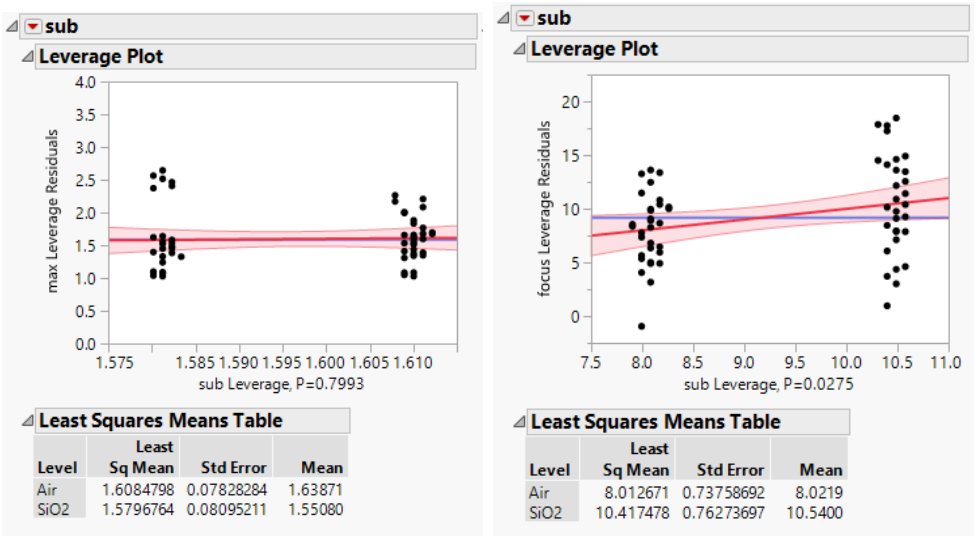

Figure 13. JMP output based on substrate material

Figure 14 includes the leverage plots for wavelength. Each shows that wavelength has an impact on both focus depth and intensity. The wavelength dependence on focus depth shows promise for multispectral pixels, but the intensity difference may have an impact on detector design.

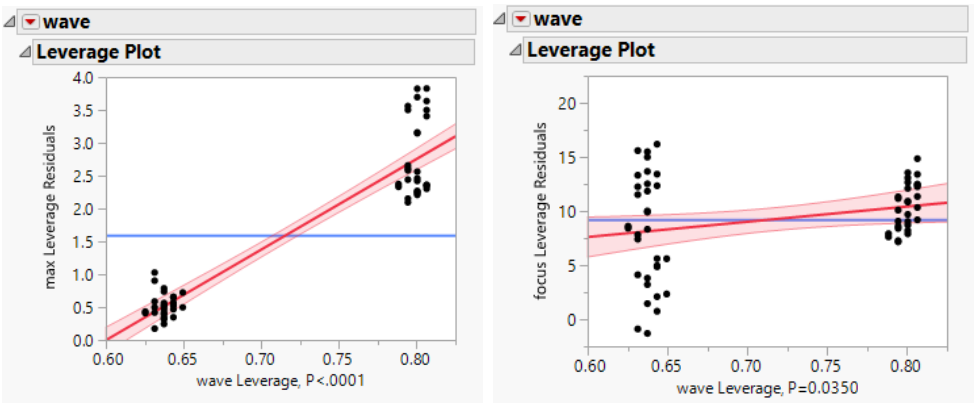

Figure 14. JMP output based on wavelength

Figure 15 shows various indicators for the maximum intensity and focus depth. The column

`"Prob > F"`

indicates the P value for each parameter. For maximum intensity, increment and wavelength demonstrated conclusive results. This indicates that changing the increment is the most effective way to adjust the transmission through the lenses. It also shows that transmission is impacted by wavelength. For focus depth, this shows that changing the number of slits is the best way to adjust the focus depth. This is in good agreement with previous work. It also show that material choice impacts focus depth. This makes intuitive sense based on standard optics principles. Finally, this shows that wavelength does impact focus depth.

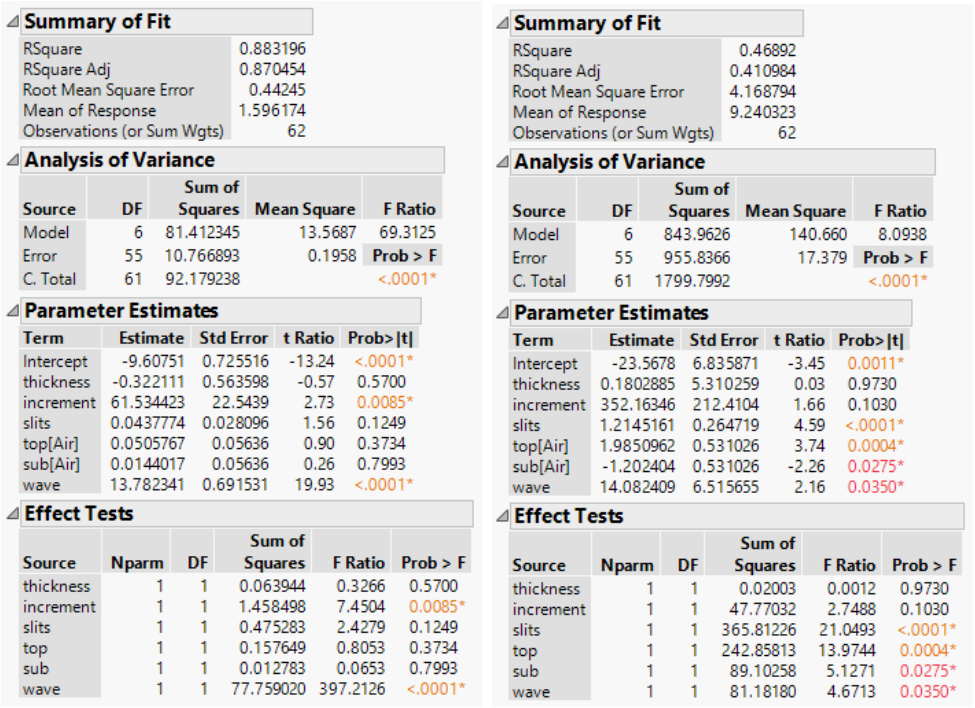

Summary of Fit

RSquare	0.883196
RSquare Adj	0.870454
Root Mean Square Error	0.44245
Mean of Response	1.596174
Observations (or Sum Wgts)	62

Analysis of Variance

Source	DF	Sum of Squares	Mean Square	F Ratio
Model	6	81.412345	13.5687	69.3125
Error	55	10.766893	0.1958	Prob > F
C. Total	61	92.179238		<.0001*

Parameter Estimates

Term	Estimate	Std Error	t Ratio	Prob>|t|
Intercept	-9.60751	0.725516	-13.24	<.0001*
thickness	-0.322111	0.563598	-0.57	0.5700
increment	61.534423	22.5439	2.73	0.0085*
slits	0.0437774	0.028096	1.56	0.1249
top[Air]	0.0505767	0.05636	0.90	0.3734
sub[Air]	0.0144017	0.05636	0.26	0.7993
wave	13.782341	0.691531	19.93	<.0001*

Effect Tests

Source	Nparm	DF	Sum of Squares	F Ratio	Prob > F
thickness	1	1	0.063944	0.3266	0.5700
increment	1	1	1.458498	7.4504	0.0085*
slits	1	1	0.475283	2.4279	0.1249
top	1	1	0.157649	0.8053	0.3734
sub	1	1	0.012783	0.0653	0.7993
wave	1	1	77.759020	397.2126	<.0001*

Summary of Fit

RSquare	0.46892
RSquare Adj	0.410984
Root Mean Square Error	4.168794
Mean of Response	9.240323
Observations (or Sum Wgts)	62

Analysis of Variance

Source	DF	Sum of Squares	Mean Square	F Ratio
Model	6	843.9626	140.660	8.0938
Error	55	955.8366	17.379	Prob > F
C. Total	61	1799.7992		<.0001*

Parameter Estimates

Term	Estimate	Std Error	t Ratio	Prob>|t|
Intercept	-23.5678	6.835871	-3.45	0.0011*
thickness	0.1802885	5.310259	0.03	0.9730
increment	352.16346	212.4104	1.66	0.1030
slits	1.2145161	0.264719	4.59	<.0001*
top[Air]	1.9850962	0.531026	3.74	0.0004*
sub[Air]	-1.202404	0.531026	-2.26	0.0275*
wave	14.082409	6.515655	2.16	0.0350*

Effect Tests

Source	Nparm	DF	Sum of Squares	F Ratio	Prob > F
thickness	1	1	0.02003	0.0012	0.9730
increment	1	1	47.77032	2.7488	0.1030
slits	1	1	365.81226	21.0493	<.0001*
top	1	1	242.85813	13.9744	0.0004*
sub	1	1	89.10258	5.1271	0.0275*
wave	1	1	81.18180	4.6713	0.0350*

Figure 15. Summary JMP output

VI. Recommendations

6.1 Software Recommendations

Because FDTD simulations are a well defined method of solving Maxwell's equations in a stepwise manner, any FDTD software should yield accurate results assuming all materials were characterized correctly. However, each software package is built for different purposes and has different strengths and weaknesses. Sentaurus EMW performed well and the Sentaurus ecosystem makes it easy to perform many simulations, so I would recommend any follow up work to use this software.

6.2 Recommendations from Results

The results can inform where effort should be spent in future work. First, it was seen that gold thickness was insignificant, so thicknesses which will allow easier manufacture should be used. The increment factor produced useful results given a linear increase in slit width. Based on the results, the increment should be made as large as is reasonable. It was found that increasing the number of slits increases the focus depth, so the number of slits will be determined based on where the absorption region will be in the sensor. The results for top material show an additional option to control the focus depth other than the grating itself.

6.3 Future Modeling

The experiment results demonstrated that the design of the lens and wavelength impact both the focus depth and the maximum intensity. This shows promise toward the end of creating multispectral pixels. The next step is to perform this experiment in the infrared. Infrared simulations were attempted, but not successful. A major

factor is that the gold is well defined in the visible spectrum, but the Lorentz-Drude model is less well defined in the infrared.

Future work could also experiment with exponential increases in slit width and differences in center slit width. Additionally, different slit profiles should be tested to determine if the sidewall profile of each slit impacts the overall performance of the grating.

Another future step is to accurately model the materials to be used in the sensors and perform simulations with those materials. This will involve modeling complex refractive index as well as absorption. This includes the substrate material and the grating material. For the grating material, multiple metals have been shown to demonstrate the plasmonic effect. Thus far, no other exotic materials have been tested to determine if additional benefit can be achieved. Towards the effort of creating multispectral pixels, materials will have to be used on the upper detector that are transparent to the wavelength with the deeper focus spot.

6.4 Experimental Validation

Once modeling produces the correct depth of focus, devices will need to be built to test the results. This will include determining a cascading arrangement of sensors which are transparent to wavelengths which focus deeper, and utilize infrared transparent conductors. With such a device available, then individual wavelengths can be introduced separately and together to ultimately determine the success of this method of modeling. An experiment similar to the experiment performed by Verslegers *et al.*, but in the infrared would be a good starting point.

Appendix A.

Command File for Sentaurus Device Editor:

```
(define goldt @goldt@)
;sets thickness of gold

(define goldw @goldw@)
;sets distance between slits to 200nm

(define centerslit @centerslit@)
;sets center slit width to 80nm

(define half (/ centerslit 2.0))

(define incr @increment@)
;slits increase by 10nm as further from center

(define numberslits @numberslits@)
;number of slits on either side of center slit

(sdegeo:create-rectangle (position -4 -40 0)...
...(position 4 0 0) "@submat@" "sub")

(sdegeo:create-rectangle (position -4 0 0)...
...(position 4 goldt 0) "Gold" "goldlayer")
```

```
(sdegeo:create-rectangle (position (- 0.0 half) 0 0)...
...(position half goldt 0) "@topmat@" "center")

(define w centerslit)
(define end half)
(define st 0)

(do ( (i 0 (+ i 1)) ) ; i is counter name, 0 initial value, (+ i 1) incrementer
    ( (= i numberslits) ) ; End Tester
    (begin   ; Body of loop
(set! w (+ w incr))
(set! st (+ end goldw))
(set! end (+ st w))
(sdegeo:create-rectangle (position st 0 0)...
...(position end goldt 0) "@topmat@" "slit")
    )
)

(set! end (- 0.0 half))
(set! w centerslit)

(do ( (i 0 (+ i 1)) ) ; i is counter name, 0 initial value, (+ i 1) incrementer
    ( (= i numberslits) ) ; End Tester
    (begin   ; Body of loop
(set! w (+ w incr))
(set! st (- end goldw))
```

```
(set! end (- st w))
(sdegeo:create-rectangle (position st 0 0)...
...(position end goldt 0) "@topmat@" "slit")
    )
)

(sdegeo:create-rectangle (position -4 goldt 0)...
...(position 4 10 0) "@topmat@" "top")



(sdeio:save-tdr-bnd (get-body-list) "basic_@node@_bnd.tdr")
```

Command File for Sentaurus Mesh:

```
Title "Basic 2D"

Controls {
}

IOControls {
InputFile = "basic_@previous@_bnd.tdr"
EnableSections
Verbosity=3
}

Tensor {
  Mesh {
```

```
    maxCellSize = .05
    minCellSize = .001

  }

  EMW {
    Parameter Filename = "mat.par"
    wavelength = @wave@
    ComplexRefractiveIndex WavelengthDep real
    Grading Off
  }
}
```

Command File for Sentaurus EMW:

```
Globals {
  GridFile        = "n@node|-2@_msh.tdr"
  ResultFile     = "@plot@"
  LogFile         = "@log@"
  ParameterFile   = "mat_vis.par"
  NumberOfThreads = 1
  Kernel          = Synopsys
  TotalTimeSteps  = 200000
}

ComplexRefractiveIndex {
  Material = "Ambient"
}
```

```
ComplexRefractiveIndex {
  Material = "Gold"
  WavelengthDep = {Real,Imag}
}

ComplexRefractiveIndex {
  Material = "Silicon"
}

ComplexRefractiveIndex {
  Material = "GaInSb"
}

DispersiveMedia {
  Material = "Gold"
  Model = DrudeModLorentz
  ModelParameters = UserDefined
  DeltaK = 0.01
  InterfaceAveraging = yes
}

ComplexRefractiveIndex {
  Material = "SiO2"
  WavelengthDep = {Real,Imag}
}
```

```
Boundary {
  Type  = @sidebound@
  Sides = {X}
}

Boundary {
  Type  = @sidebound@
  Sides = {Y}
}



PlaneWaveExcitation {
  BoxCorner1 = {-5,9,0}
  BoxCorner2 = {5,9,0}
  Theta      = 90
  Phi      = 270
  Psi        = 90
  Wavelength = @<1000.*wave>@ * nm
  Intensity  = 0.1  * W/cm2
  Nrise      = 1    * number of signal periods until full power
}

Plot {
  Name = "n@node@_Eabs"
  Quantity  = {AbsElectricField, AbsMagneticField, Region}
```

```
  TickStep  = 5000
  StartTick = 10000
  EndTick   = 45000
  FinalPlot = yes
}

Save {
  Name = "@save@"
  Quantity = {AbsorbedPhotonDensity, PowerFluxDensity}
}

Detector {
  Tolerance = 1e-4
}
```

Command File for Sentaurus Visual:

```
load_file /home/ENG/ge18m/pkennedy/TCAD/basic2D/n@previous@_Eabs_eml.tdr
create_plot -dataset n@previous@_Eabs_eml
select_plots {Plot_n@previous@_Eabs_eml}

set_field_prop -plot Plot_n@previous@_Eabs_eml -geom
n@previous@_Eabs_eml Abs(AbsMagneticField-V) -show_bands

set_field_prop -plot Plot_n@previous@_Eabs_eml -geom
n@previous@_Eabs_eml Abs(AbsMagneticField-V) -max 3 -max_fixed
```

```
export_view /home/ENG/ge18m/pkennedy/PLOTS/n@previous@_Eabs_eml_Image.png
-plots {Plot_n@previous@_Eabs_eml} -

format png -resolution 1133x916



create_cutline -plot Plot_n@previous@_Eabs_eml -type x -at 0
create_plot -dataset C1(n@previous@_Eabs_eml) -1d
select_plots {Plot_C1(n@previous@_Eabs_eml)}
create_curve -plot Plot_C1(n@previous@_Eabs_eml)
-dataset {C1(n@previous@_Eabs_eml)} -axisX Y -axisY Abs(AbsMagneticField-V)

zoom_plot -plot Plot_C1(n@previous@_Eabs_eml) -window {-30 0 0 3}

export_view /home/ENG/ge18m/pkennedy/PLOTS/n@previous@_Eabs_eml_Cutline.png
-plots {Plot_C1(n@previous@_Eabs_eml)}

-format png -resolution 1133x916

export_curves {Curve_1} -plot Plot_C1(n@previous@_Eabs_eml)
-filename /home/ENG/ge18m/pkennedy/XYData/n@previous@_cutlineData.csv -format csv

exit 1
```

Appendix B.

In the following figures, the heat map of absolute value of the magnetic field is shown with a cut-line plot of the absolute value of the magnetic field along the center. This is done to demonstrate a visual representation of which lenses have the highest transmission. The peak of the cut-line plot presents a visual representation of the focus depth for each plasmonic lens.

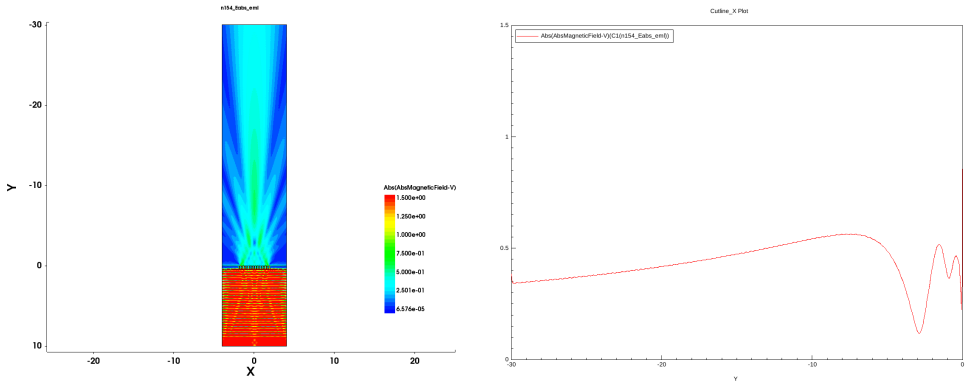

Figure B-1. Results for 400nm gold thickness, 10nm increment,and 13 slits with Air top and Air bottom at 637 nm

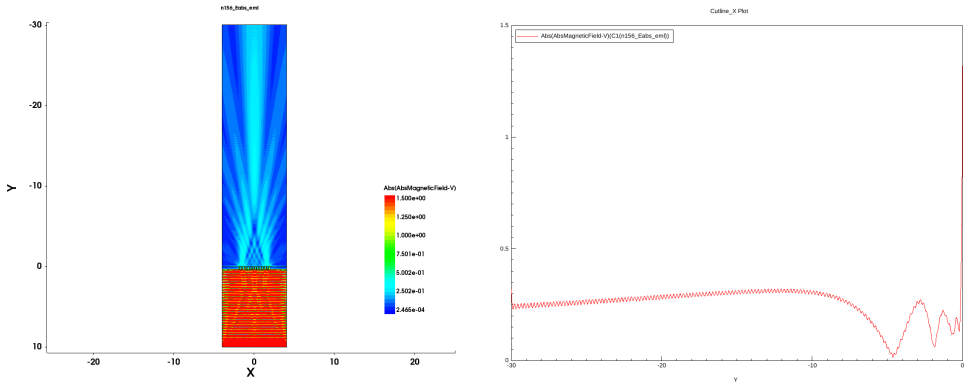

Figure B-2. Results for 400nm gold thickness, 10nm increment,and 13 slits with Air top and SiO_2 bottom at 637 nm

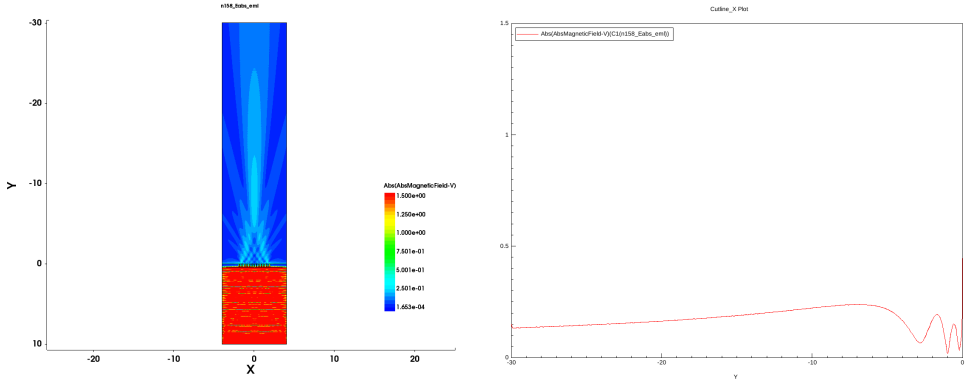

Figure B-3. Results for 400nm gold thickness, 10nm increment,and 13 slits with SiO_2 top and Air bottom at 637 nm

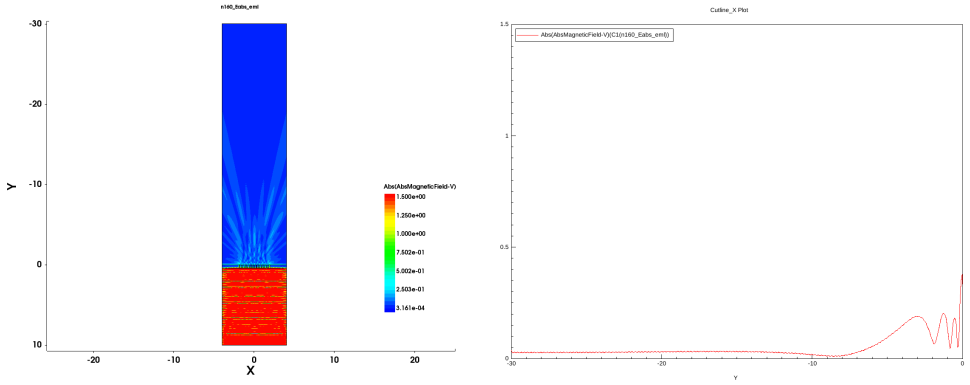

Figure B-4. Results for 400nm gold thickness, 10nm increment,and 13 slits with SiO_2 top and SiO_2 bottom at 637 nm

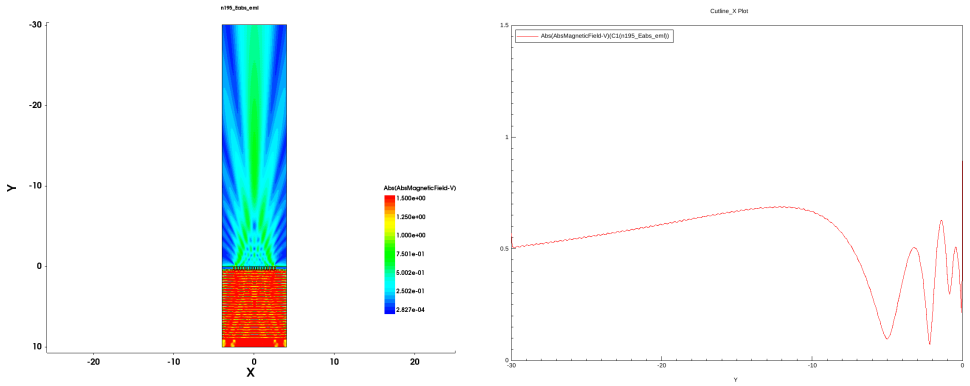

Figure B-5. Results for 400nm gold thickness, 10nm increment,and 17 slits with Air top and Air bottom at 637 nm

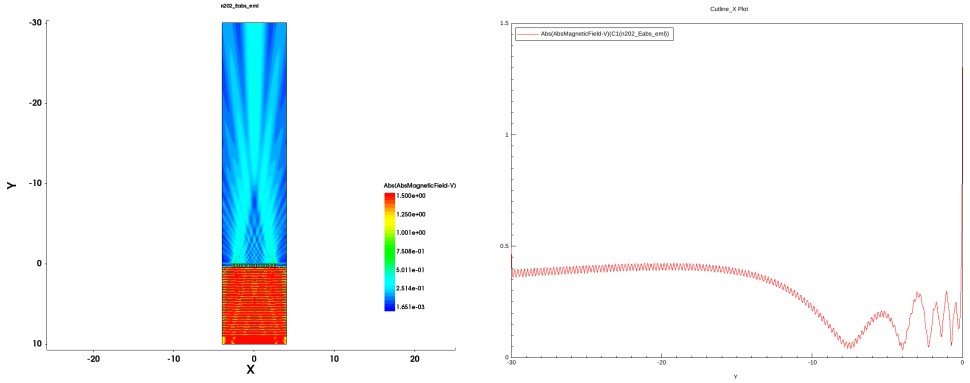

Figure B-6. Results for 400nm gold thickness, 10nm increment,and 17 slits with Air top and SiO_2 bottom at 637 nm

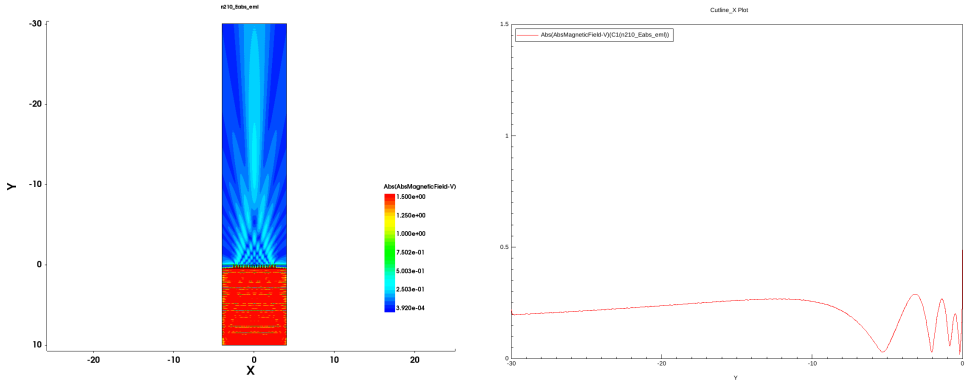

Figure B-7. Results for 400nm gold thickness, 10nm increment,and 17 slits with SiO_2 top and Air bottom at 637 nm

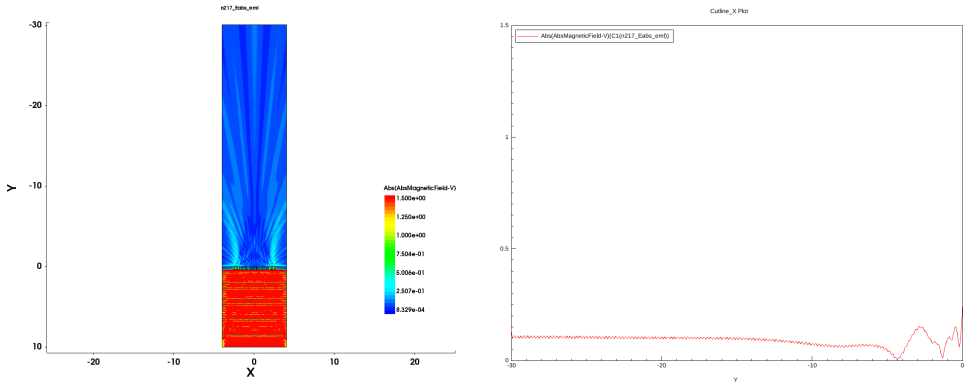

Figure B-8. Results for 400nm gold thickness, 10nm increment,and 17 slits with SiO_2 top and SiO_2 bottom at 637 nm

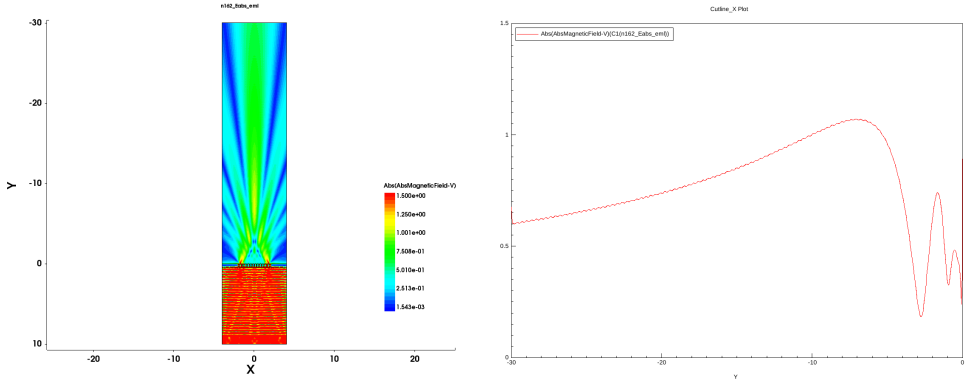

Figure B-9. Results for 400nm gold thickness, 15nm increment,and 13 slits with Air top and Air bottom at 637 nm

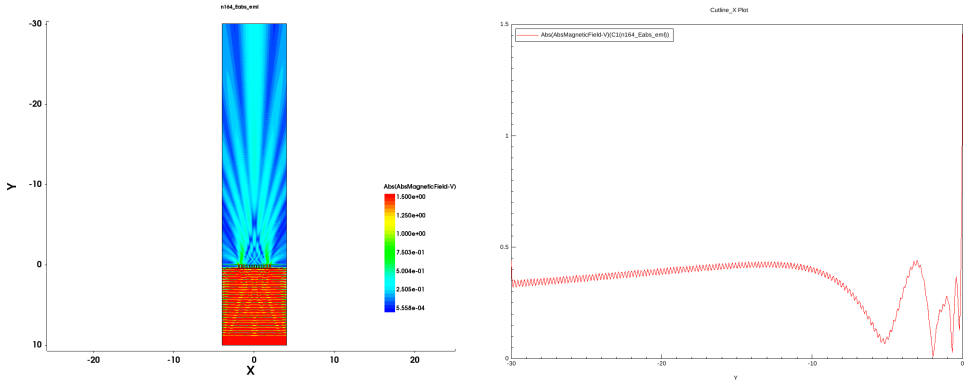

Figure B-10. Results for 400nm gold thickness, 15nm increment,and 13 slits with Air top and SiO_2 bottom at 637 nm

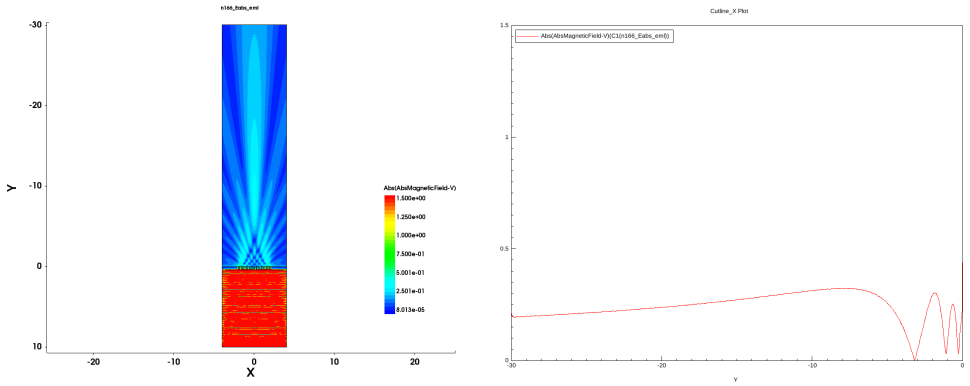

Figure B-11. Results for 400nm gold thickness, 15nm increment,and 13 slits with SiO_2 top and Air bottom at 637 nm

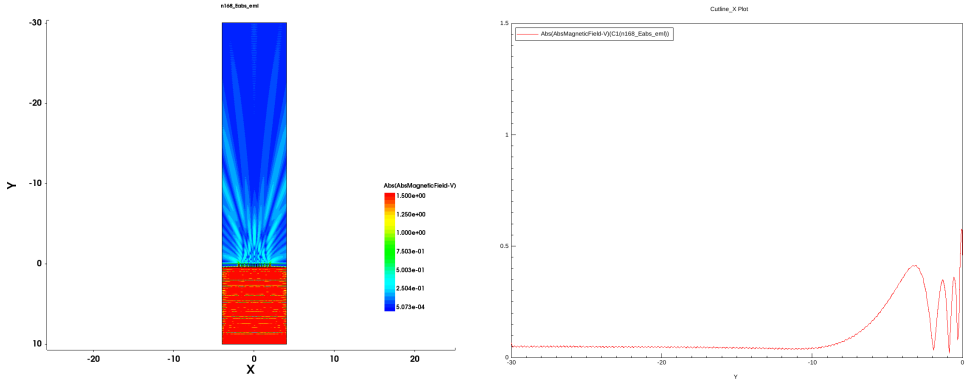

Figure B-12. Results for 400nm gold thickness, 15nm increment,and 13 slits with SiO_2 top and SiO_2 bottom at 637 nm

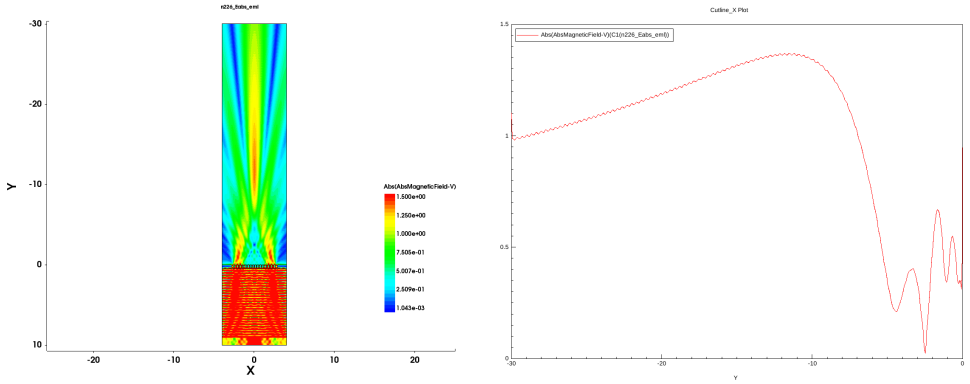

Figure B-13. Results for 400nm gold thickness, 15nm increment,and 17 slits with Air top and Air bottom at 637 nm

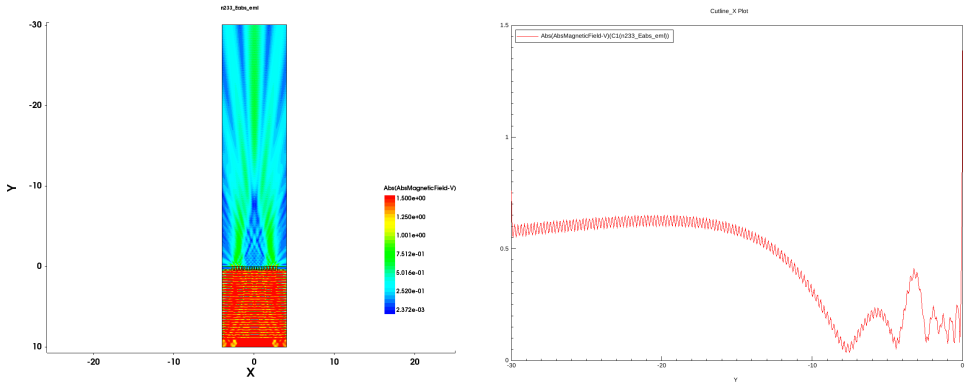

Figure B-14. Results for 400nm gold thickness, 15nm increment,and 17 slits with Air top and SiO_2 bottom at 637 nm

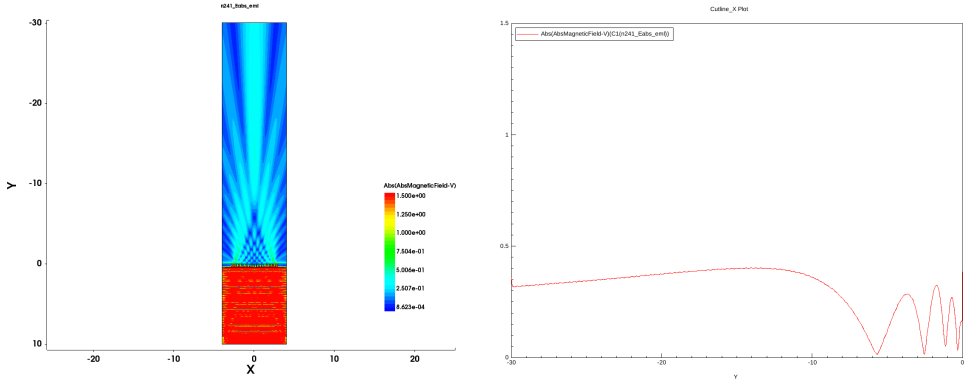

Figure B-15. Results for 400nm gold thickness, 15nm increment,and 17 slits with SiO_2 top and Air bottom at 637 nm

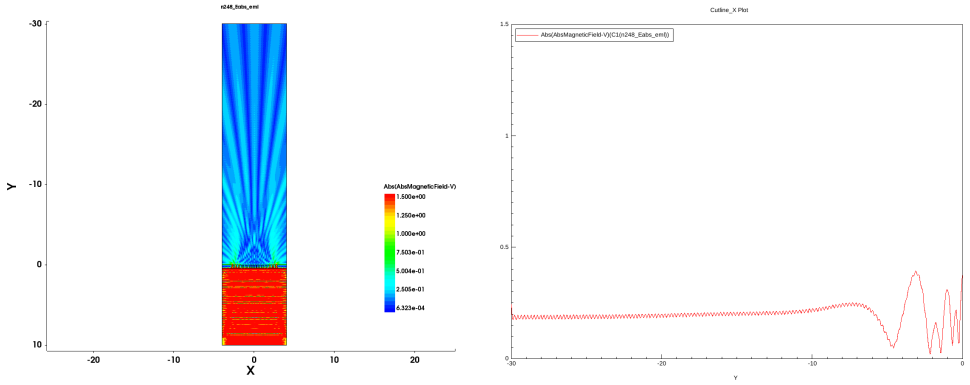

Figure B-16. Results for 400nm gold thickness, 15nm increment,and 17 slits with SiO_2 top and SiO_2 bottom at 637 nm

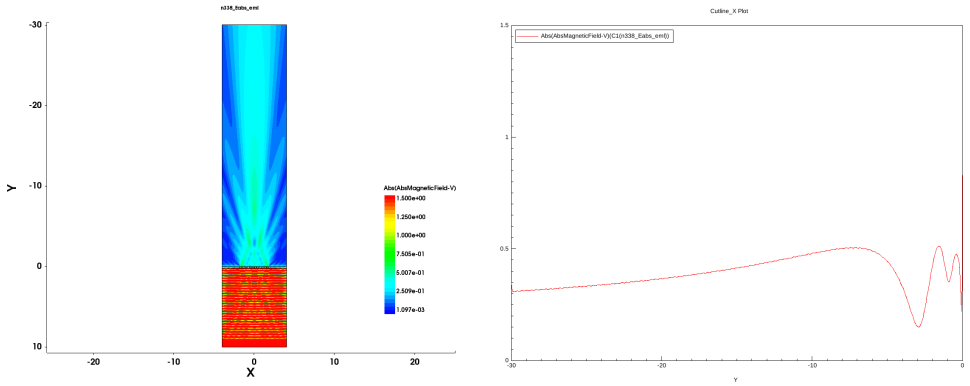

Figure B-17. Results for 200nm gold thickness, 10nm increment,and 13 slits with Air top and Air bottom at 637 nm

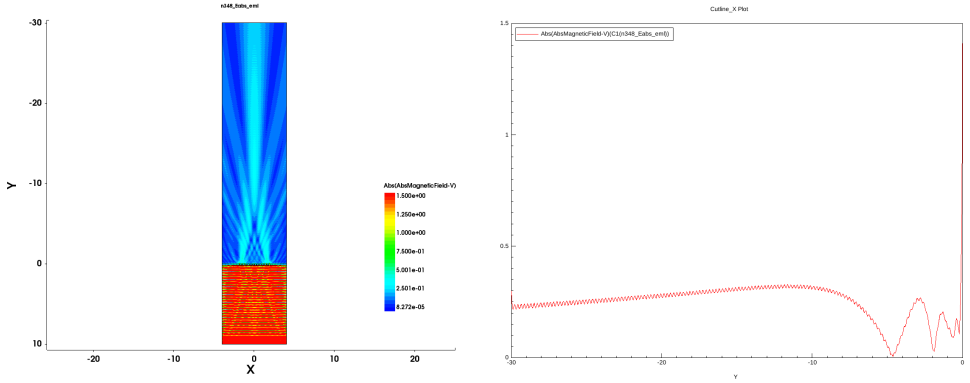

Figure B-18. Results for 400nm gold thickness, 10nm increment,and 13 slits with Air top and SiO_2 bottom at 637 nm

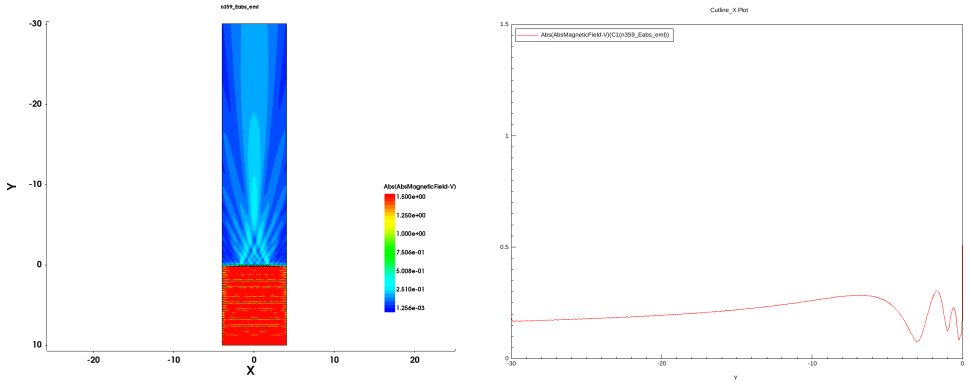

Figure B-19. Results for 400nm gold thickness, 10nm increment,and 13 slits with SiO_2 top and Air bottom at 637 nm

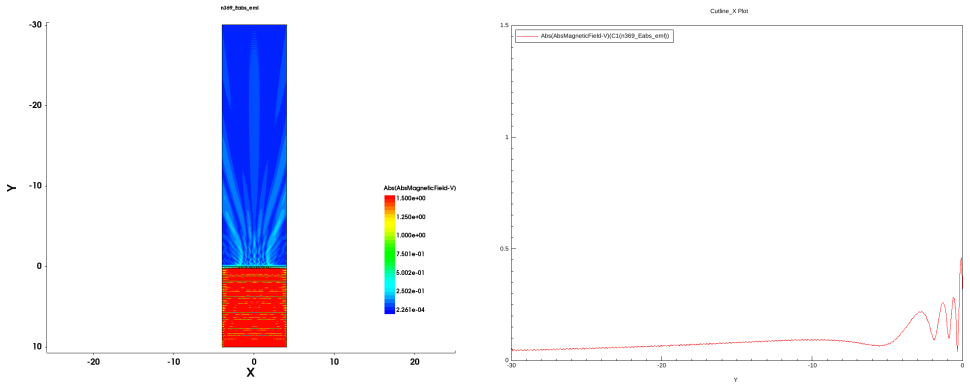

Figure B-20. Results for 400nm gold thickness, 10nm increment,and 13 slits with SiO_2 top and SiO_2 bottom at 637 nm

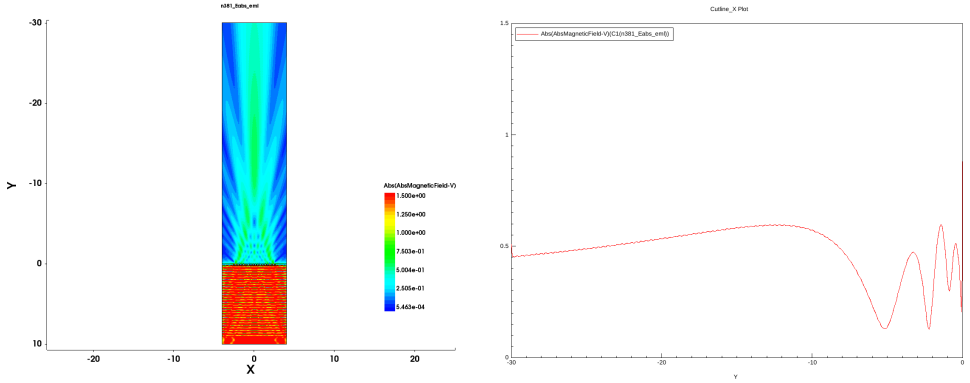

Figure B-21. Results for 400nm gold thickness, 10nm increment,and 17 slits with Air top and Air bottom at 637 nm

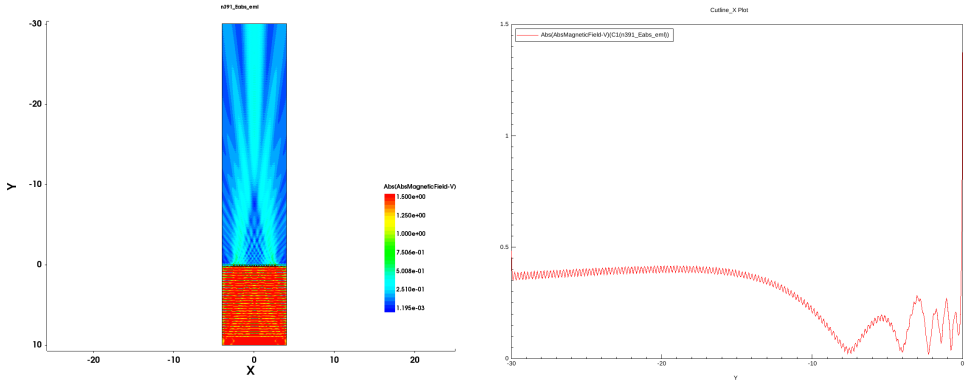

Figure B-22. Results for 200nm gold thickness, 10nm increment,and 17 slits with Air top and SiO_2 bottom at 637 nm

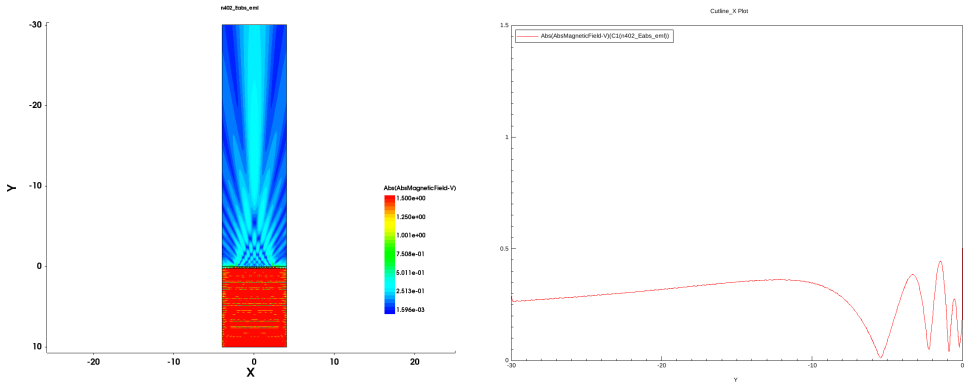

Figure B-23. Results for 400nm gold thickness, 10nm increment,and 17 slits with SiO_2 top and Air bottom at 637 nm

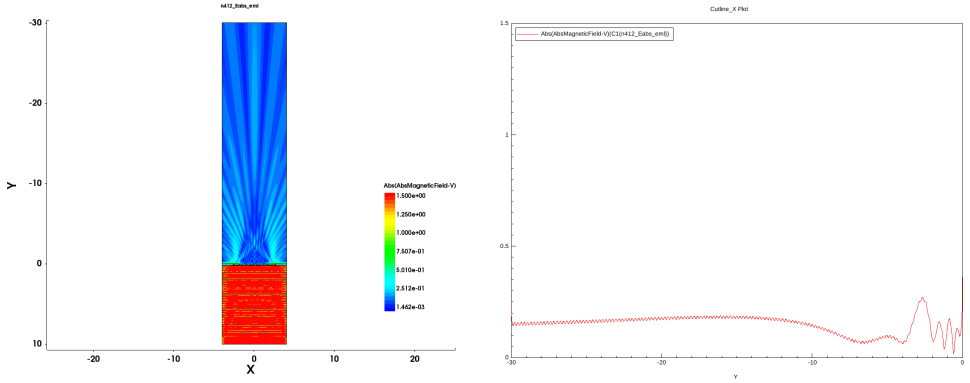

Figure B-24. Results for 400nm gold thickness, 10nm increment,and 17 slits with SiO_2 top and SiO_2 bottom at 637 nm

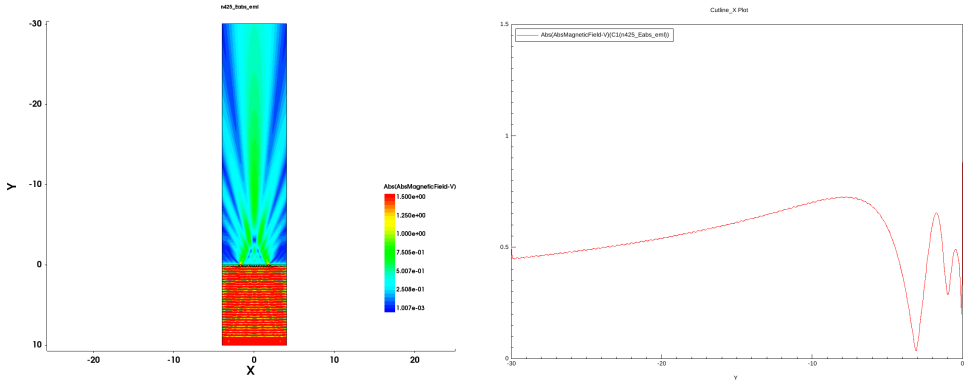

Figure B-25. Results for 200nm gold thickness, 15nm increment,and 13 slits with Air top and Air bottom at 637 nm

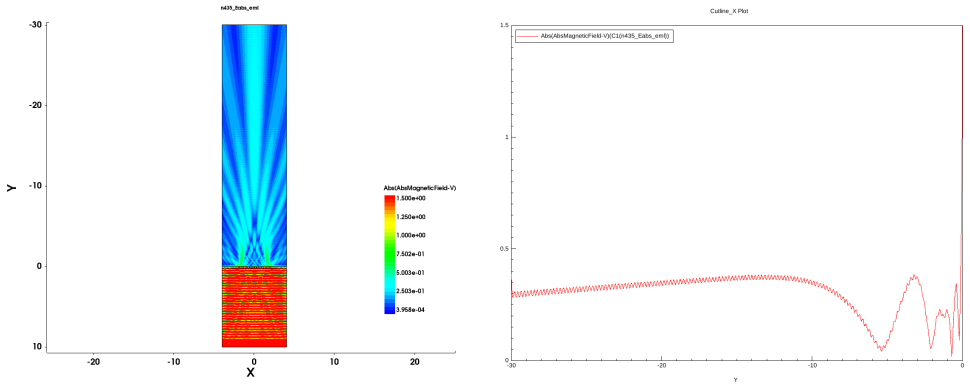

Figure B-26. Results for 400nm gold thickness, 15nm increment,and 13 slits with Air top and SiO_2 bottom at 637 nm

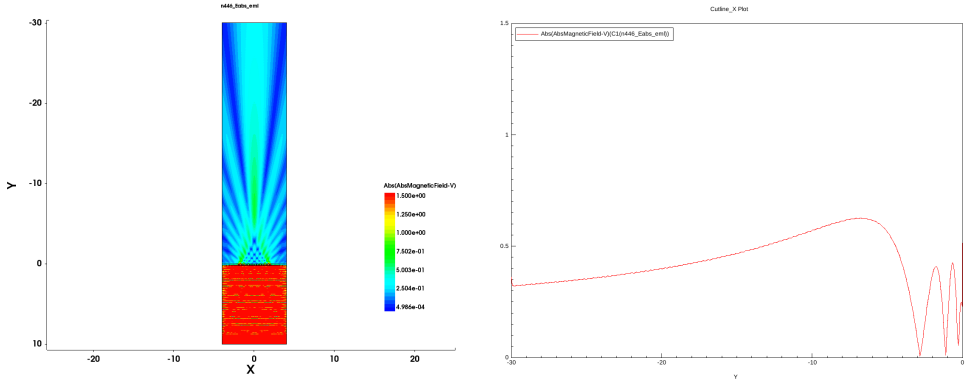

Figure B-27. Results for 400nm gold thickness, 15nm increment,and 13 slits with SiO_2 top and Air bottom at 637 nm

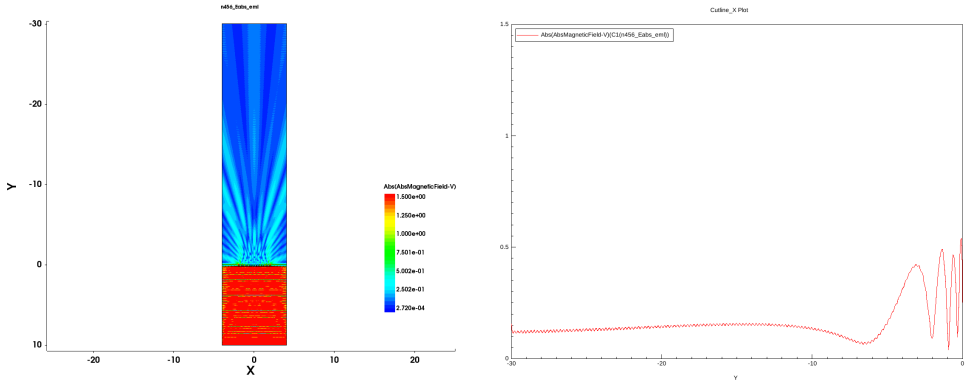

Figure B-28. Results for 400nm gold thickness, 15nm increment,and 13 slits with SiO_2 top and SiO_2 bottom at 637 nm

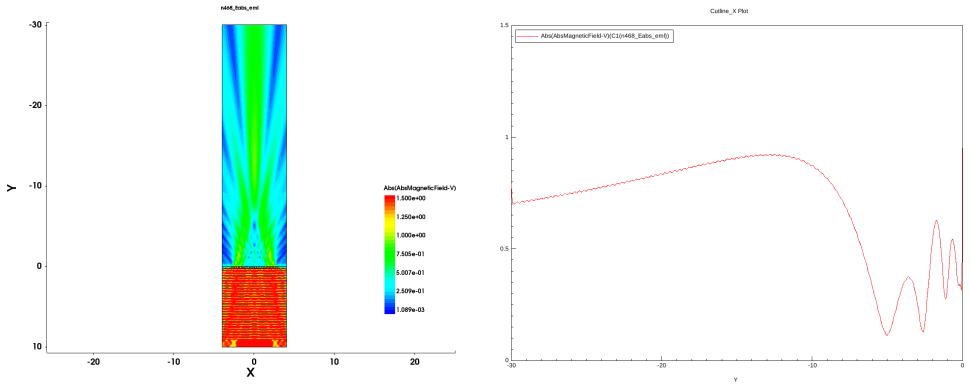

Figure B-29. Results for 200nm gold thickness, 15nm increment,and 17 slits with Air top and Air bottom at 637 nm

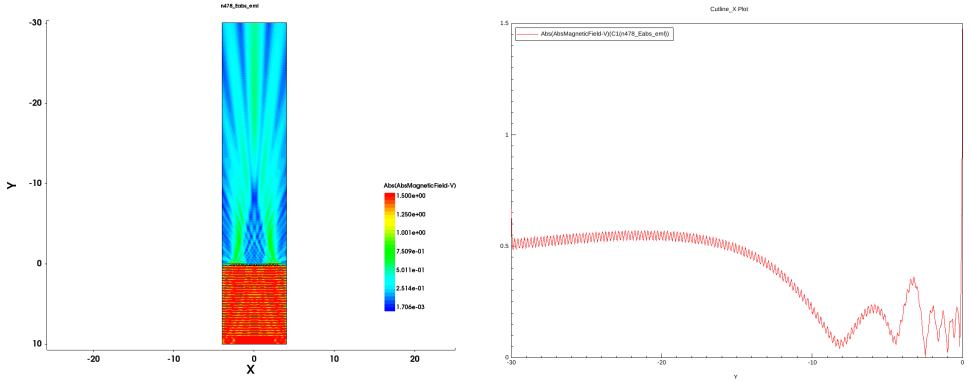

Figure B-30. Results for 400nm gold thickness, 15nm increment,and 17 slits with Air top and SiO_2 bottom at 637 nm

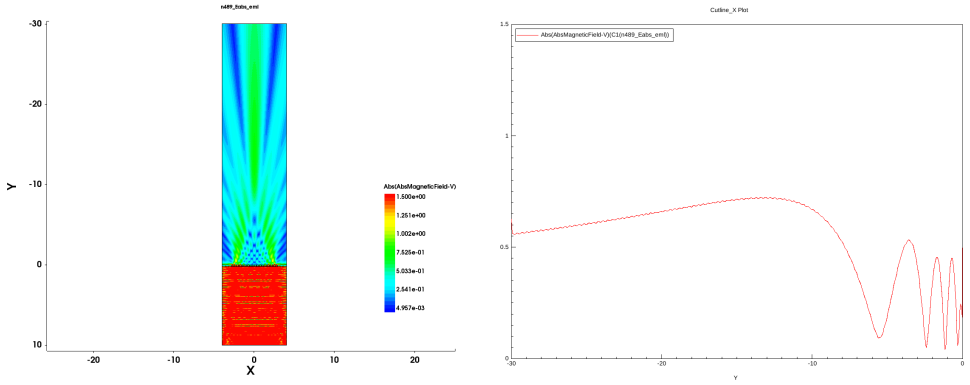

Figure B-31. Results for 400nm gold thickness, 15nm increment,and 17 slits with SiO_2 top and Air bottom at 637 nm

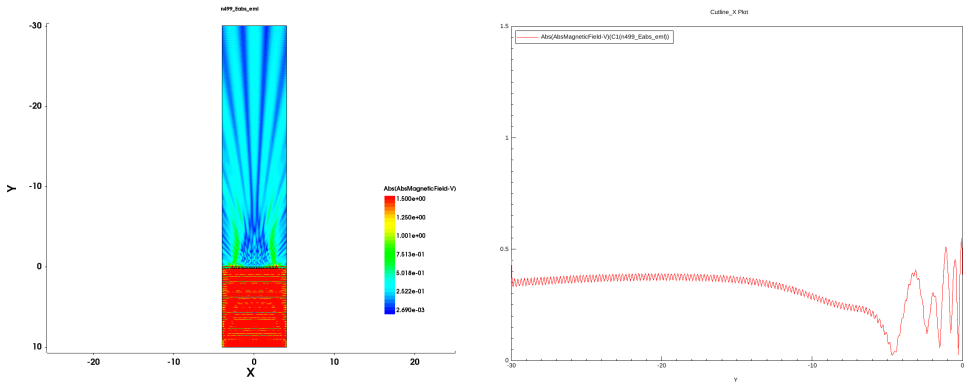

Figure B-32. Results for 400nm gold thickness, 15nm increment,and 17 slits with SiO_2 top and SiO_2 bottom at 637 nm

Appendix C.

In the following figures, the heat map of absolute value of the magnetic field is shown with a cut-line plot of the absolute value of the magnetic field along the center. This is done to demonstrate a visual representation of which lenses have the highest transmission. The peak of the cut-line plot presents a visual representation of the focus depth for each plasmonic lens.

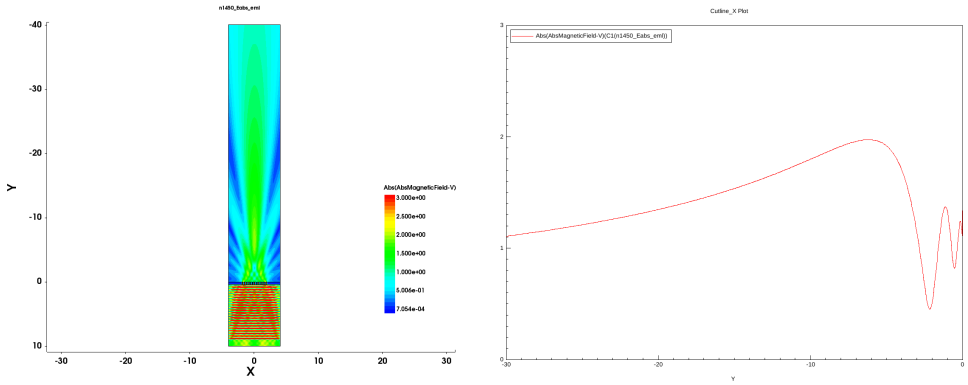

Figure C-1. Results for 400nm gold thickness, 10nm increment,and 13 slits with Air top and Air bottom at 800 nm

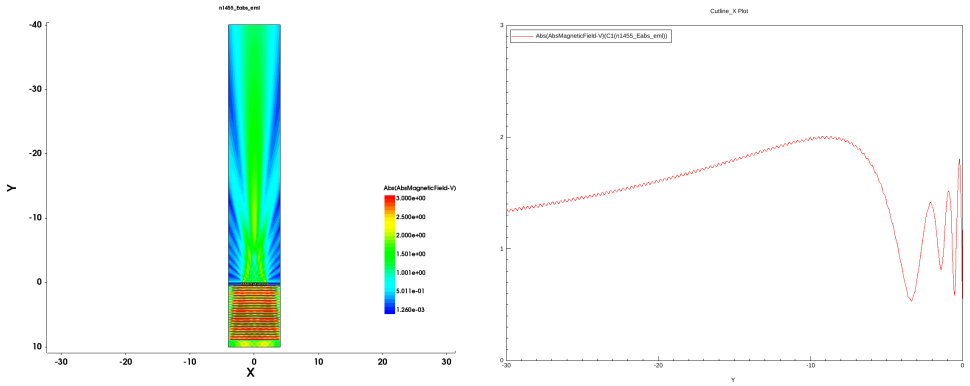

Figure C-2. Results for 400nm gold thickness, 10nm increment,and 13 slits with Air top and SiO_2 bottom at 800 nm

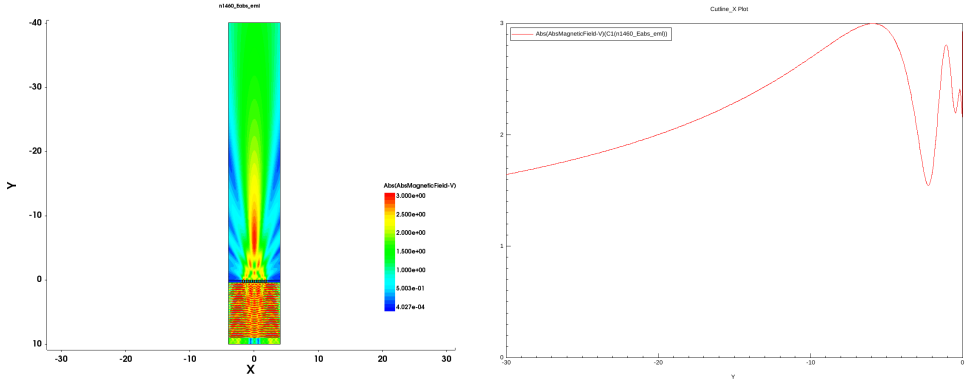

Figure C-3. Results for 400nm gold thickness, 10nm increment,and 13 slits with SiO_2 top and Air bottom at 800 nm

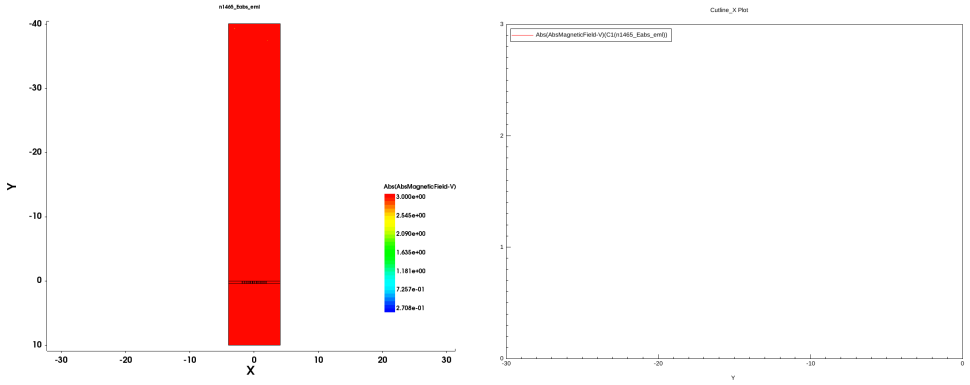

Figure C-4. Results for 400nm gold thickness, 10nm increment,and 13 slits with SiO_2 top and SiO_2 bottom at 800 nm

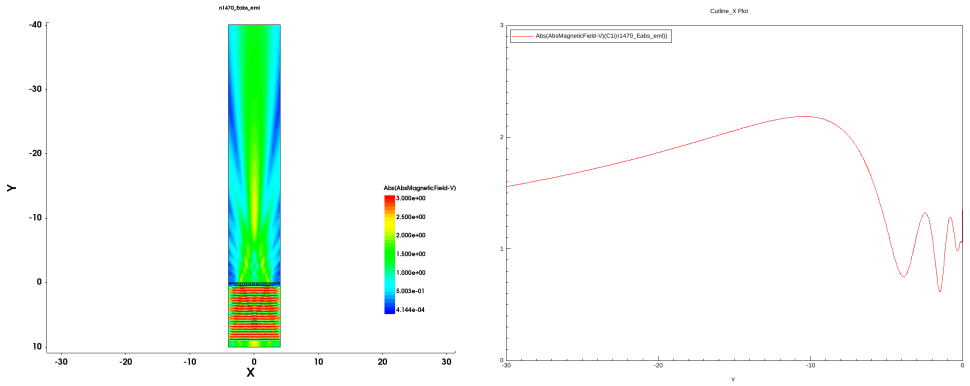

Figure C-5. Results for 400nm gold thickness, 10nm increment,and 17 slits with Air top and Air bottom at 800 nm

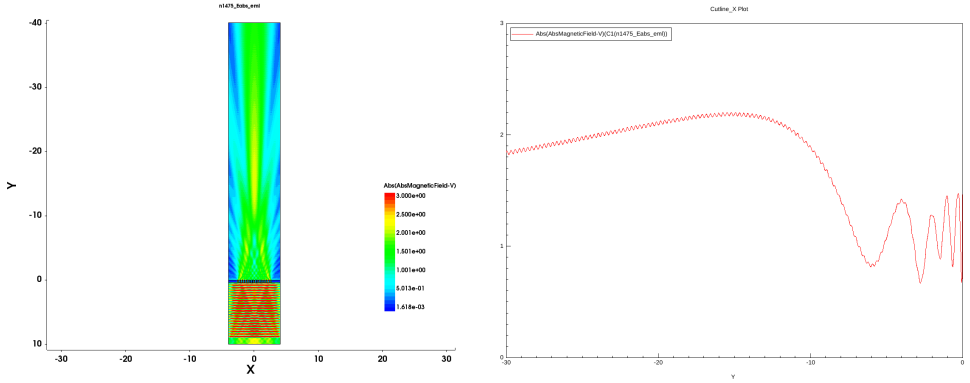

Figure C-6. Results for 400nm gold thickness, 10nm increment,and 17 slits with Air top and SiO_2 bottom at 800 nm

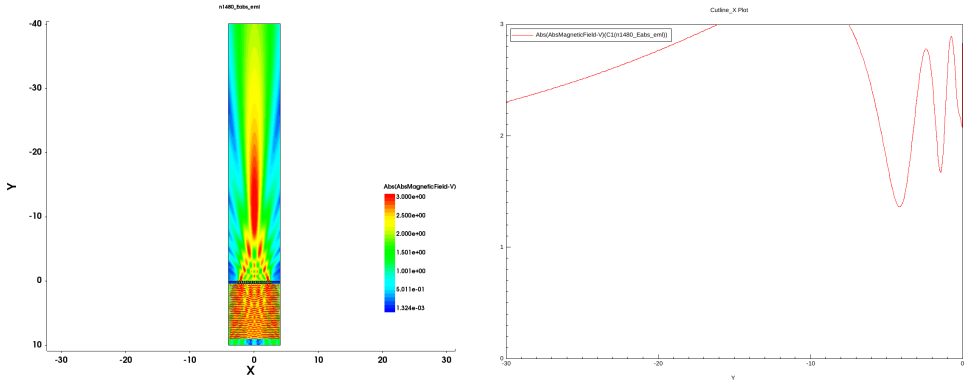

Figure C-7. Results for 400nm gold thickness, 10nm increment,and 17 slits with SiO_2 top and Air bottom at 800 nm

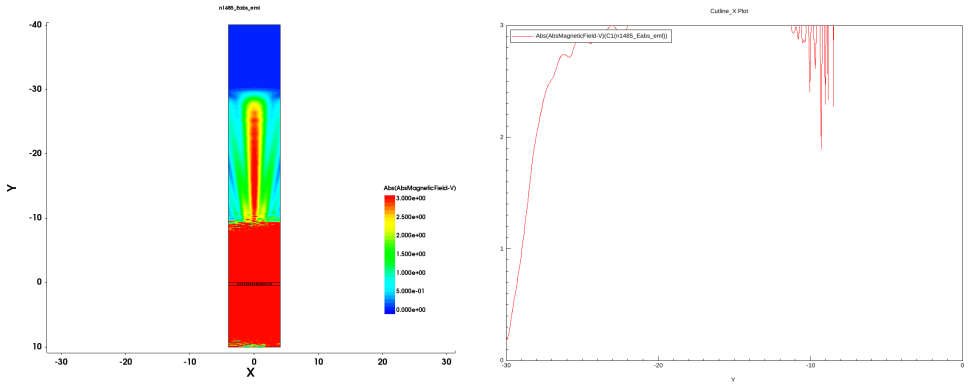

Figure C-8. Results for 400nm gold thickness, 10nm increment,and 17 slits with SiO_2 top and SiO_2 bottom at 800 nm

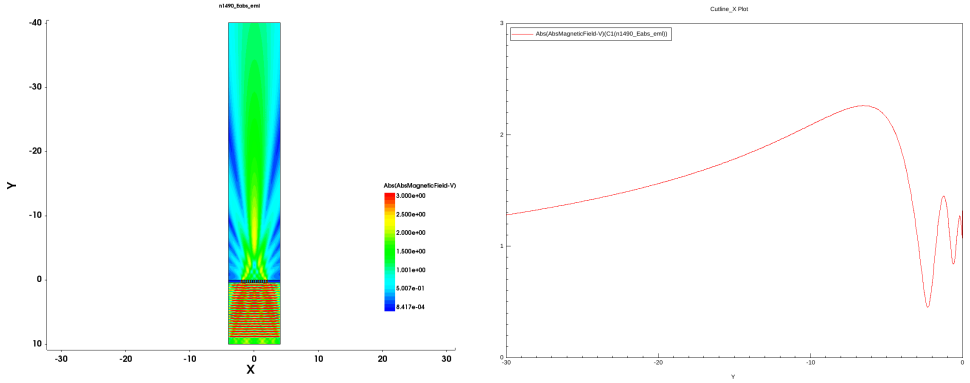

Figure C-9. Results for 400nm gold thickness, 15nm increment,and 13 slits with Air top and Air bottom at 800 nm

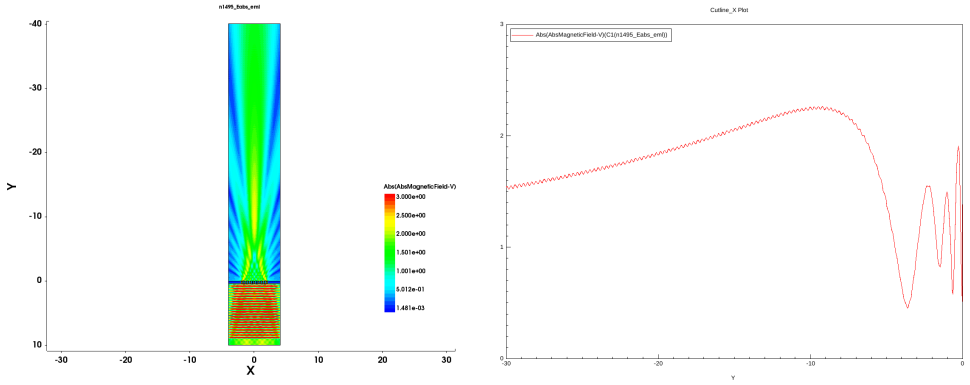

Figure C-10. Results for 400nm gold thickness, 15nm increment,and 13 slits with Air top and SiO_2 bottom at 800 nm

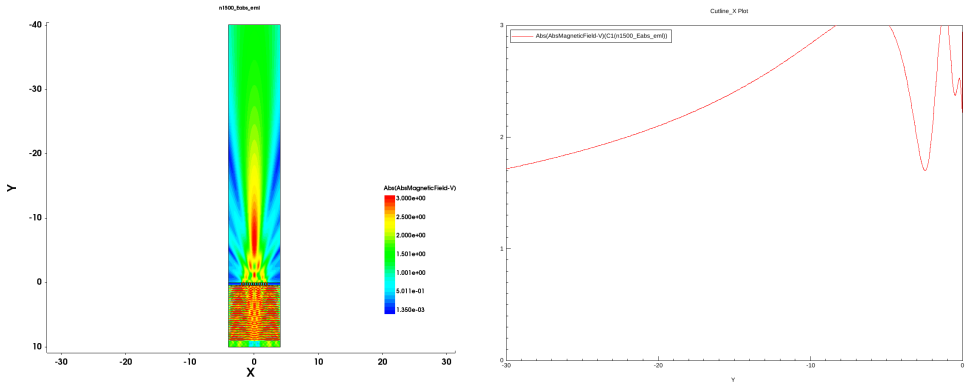

Figure C-11. Results for 400nm gold thickness, 15nm increment,and 13 slits with SiO_2 top and Air bottom at 800 nm

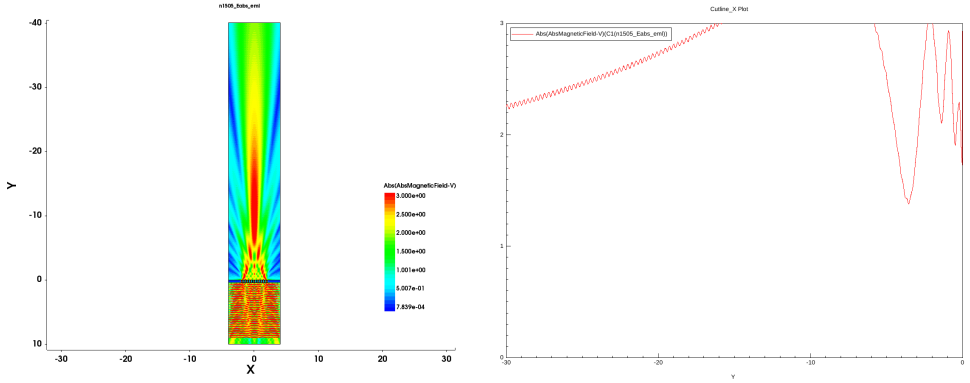

Figure C-12. Results for 400nm gold thickness, 15nm increment,and 13 slits with SiO_2 top and SiO_2 bottom at 800 nm

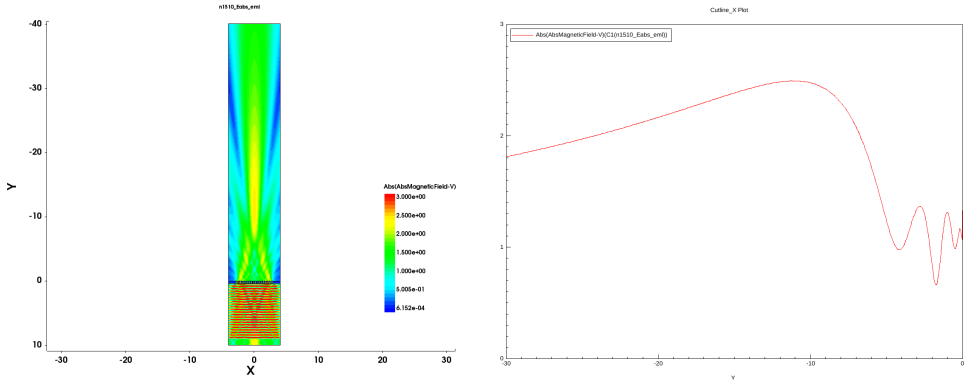

Figure C-13. Results for 400nm gold thickness, 15nm increment,and 17 slits with Air top and Air bottom at 800 nm

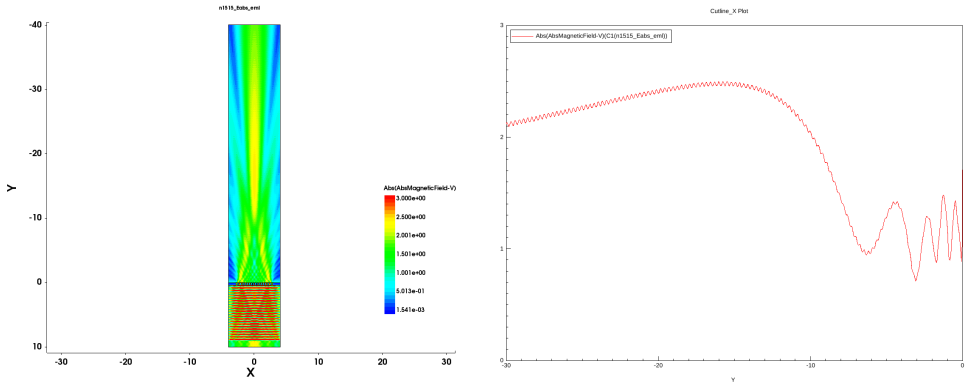

Figure C-14. Results for 400nm gold thickness, 15nm increment,and 17 slits with Air top and SiO_2 bottom at 800 nm

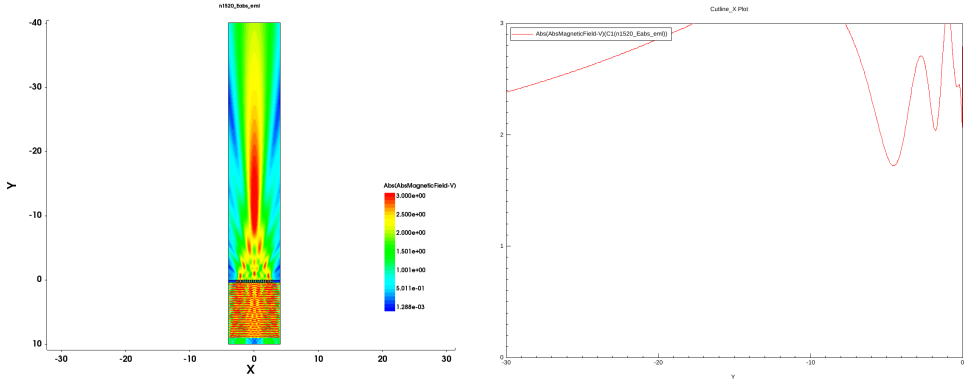

Figure C-15. Results for 400nm gold thickness, 15nm increment,and 17 slits with SiO_2 top and Air bottom at 800 nm

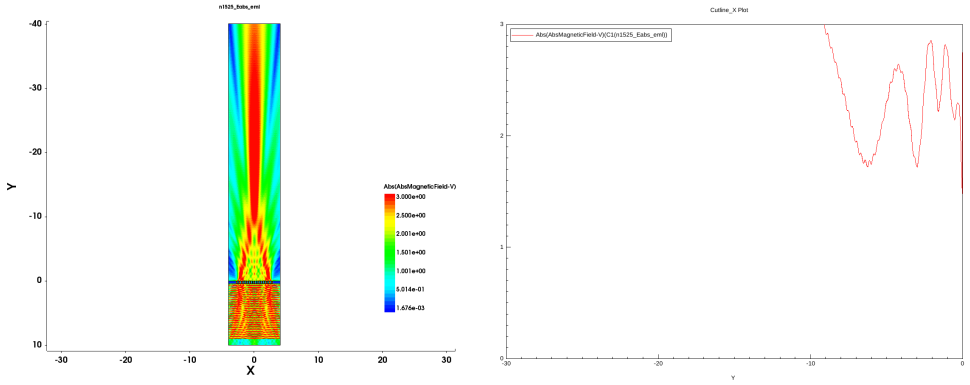

Figure C-16. Results for 400nm gold thickness, 15nm increment,and 17 slits with SiO_2 top and SiO_2 bottom at 800 nm

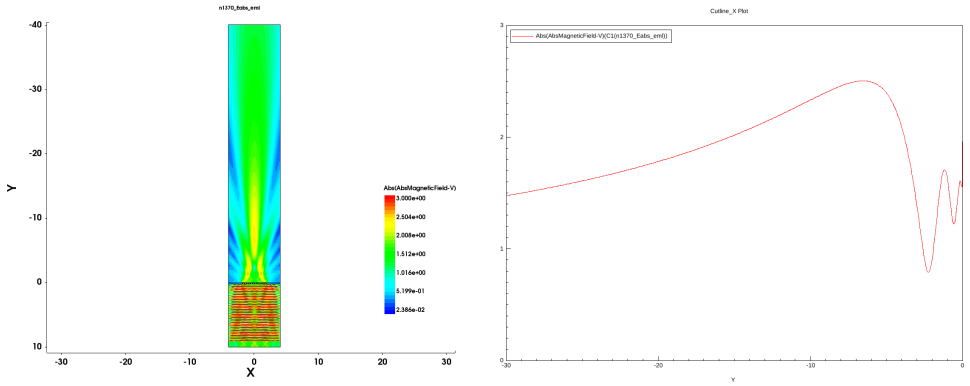

Figure C-17. Results for 200nm gold thickness, 10nm increment,and 13 slits with Air top and Air bottom at 800 nm

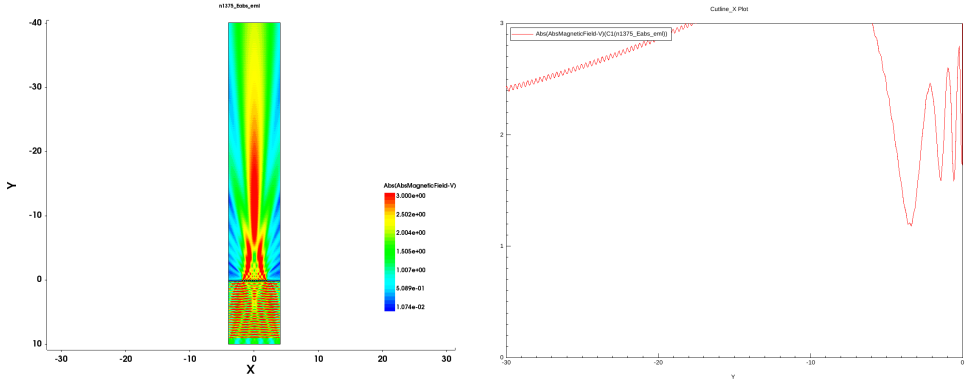

Figure C-18. Results for 400nm gold thickness, 10nm increment,and 13 slits with Air top and SiO_2 bottom at 800 nm

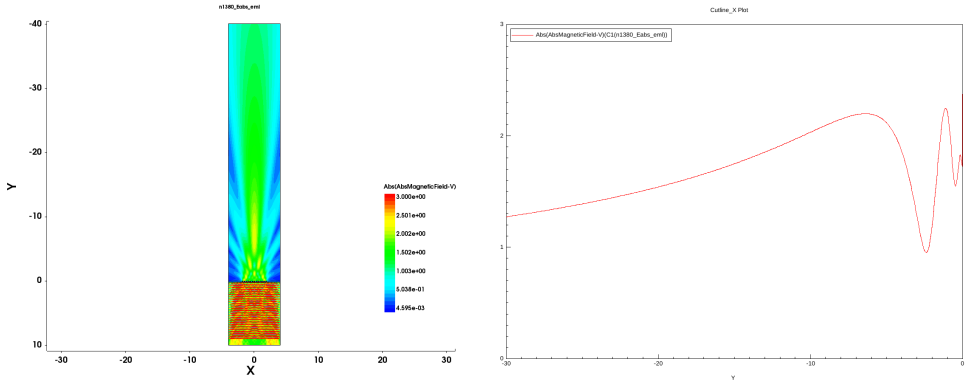

Figure C-19. Results for 400nm gold thickness, 10nm increment,and 13 slits with SiO_2 top and Air bottom at 800 nm

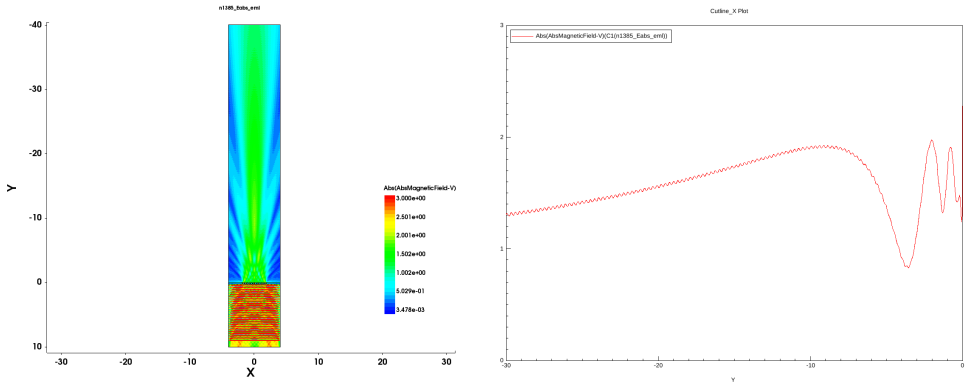

Figure C-20. Results for 400nm gold thickness, 10nm increment,and 13 slits with SiO_2 top and SiO_2 bottom at 800 nm

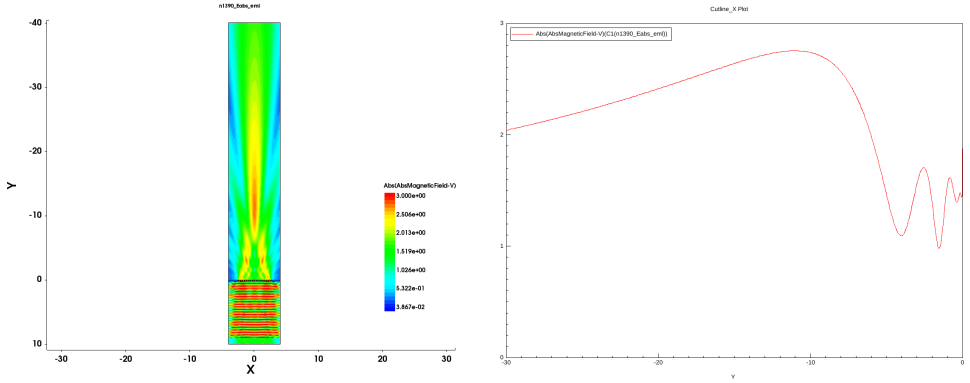

Figure C-21. Results for 400nm gold thickness, 10nm increment,and 17 slits with Air top and Air bottom at 800 nm

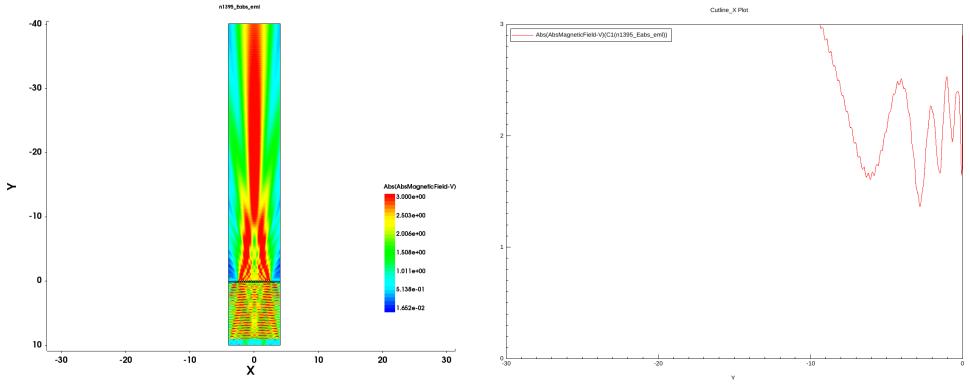

Figure C-22. Results for 200nm gold thickness, 10nm increment,and 17 slits with Air top and SiO_2 bottom at 800 nm

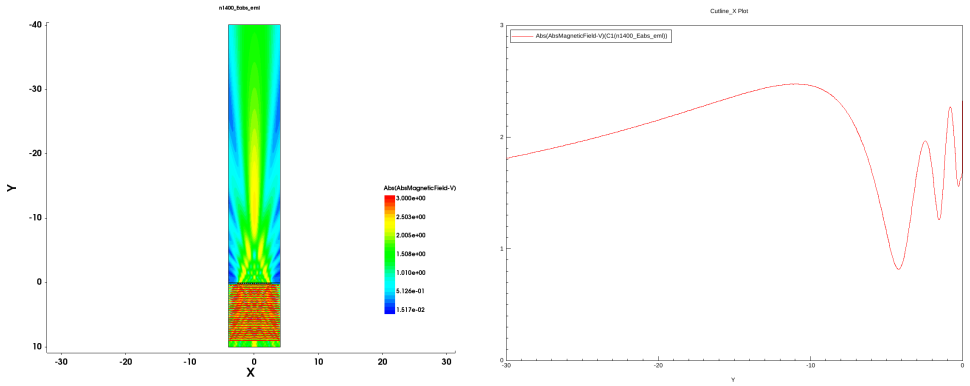

Figure C-23. Results for 400nm gold thickness, 10nm increment,and 17 slits with SiO_2 top and Air bottom at 800 nm

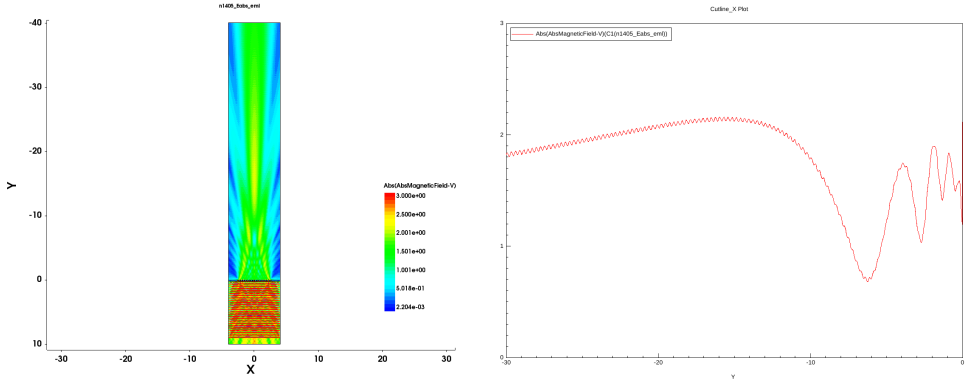

Figure C-24. Results for 400nm gold thickness, 10nm increment,and 17 slits with SiO_2 top and SiO_2 bottom at 800 nm

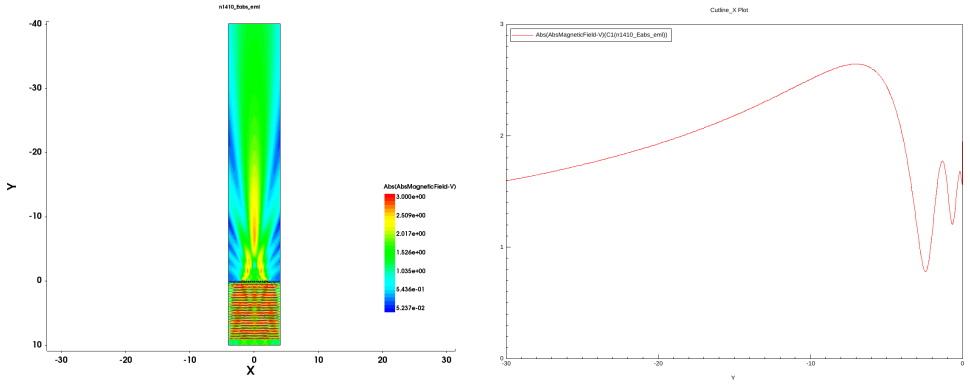

Figure C-25. Results for 200nm gold thickness, 15nm increment,and 13 slits with Air top and Air bottom at 800 nm

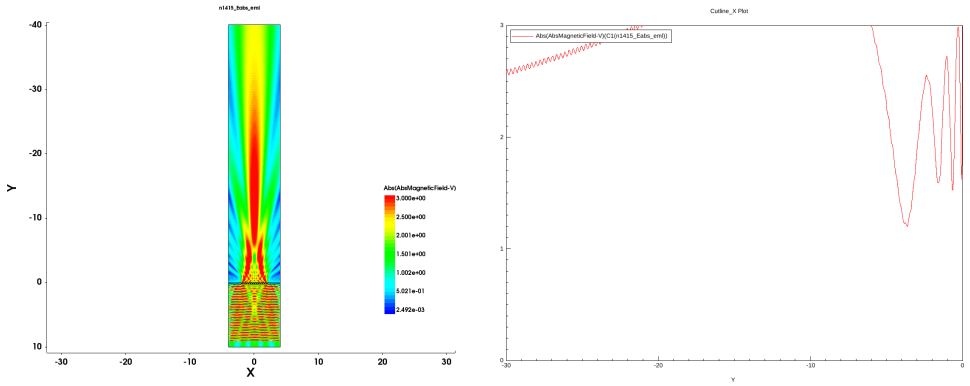

Figure C-26. Results for 400nm gold thickness, 15nm increment,and 13 slits with Air top and SiO_2 bottom at 800 nm

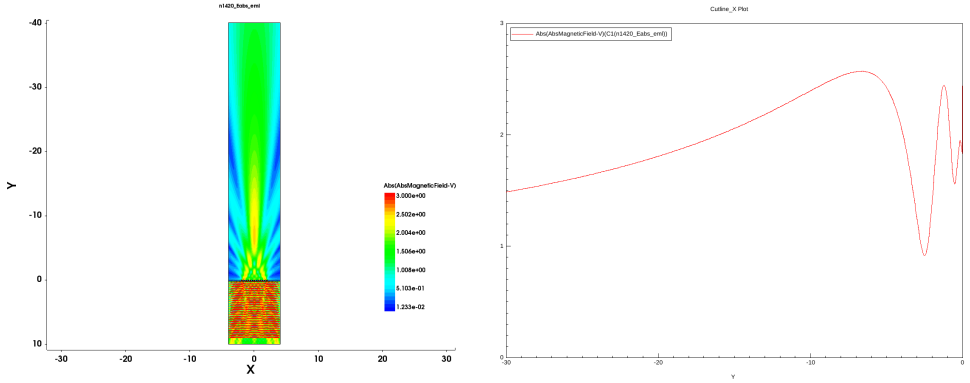

Figure C-27. Results for 400nm gold thickness, 15nm increment,and 13 slits with SiO_2 top and Air bottom at 800 nm

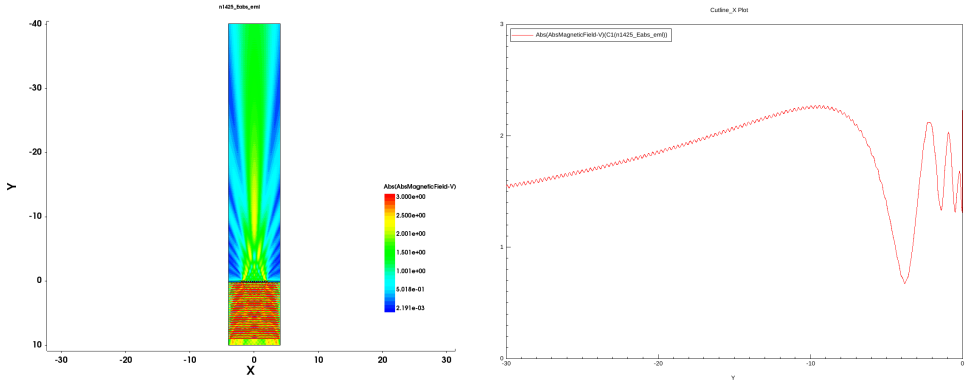

Figure C-28. Results for 400nm gold thickness, 15nm increment,and 13 slits with SiO_2 top and SiO_2 bottom at 800 nm

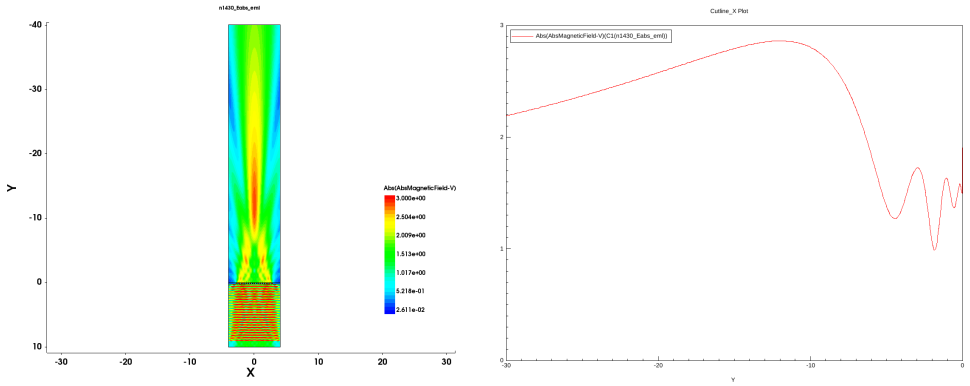

Figure C-29. Results for 200nm gold thickness, 15nm increment,and 17 slits with Air top and Air bottom at 800 nm

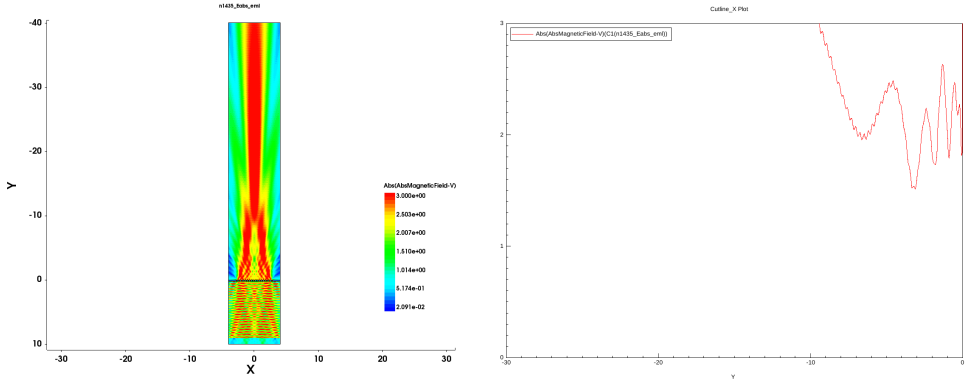

Figure C-30. Results for 400nm gold thickness, 15nm increment,and 17 slits with Air top and SiO_2 bottom at 800 nm

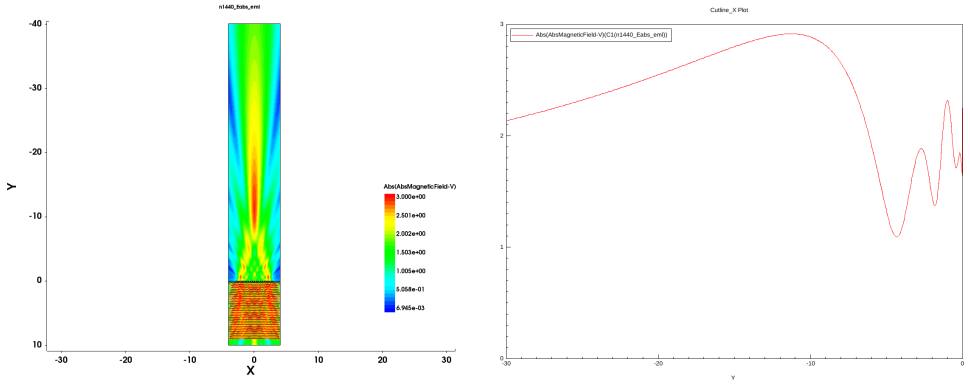

Figure C-31. Results for 400nm gold thickness, 15nm increment,and 17 slits with SiO_2 top and Air bottom at 800 nm

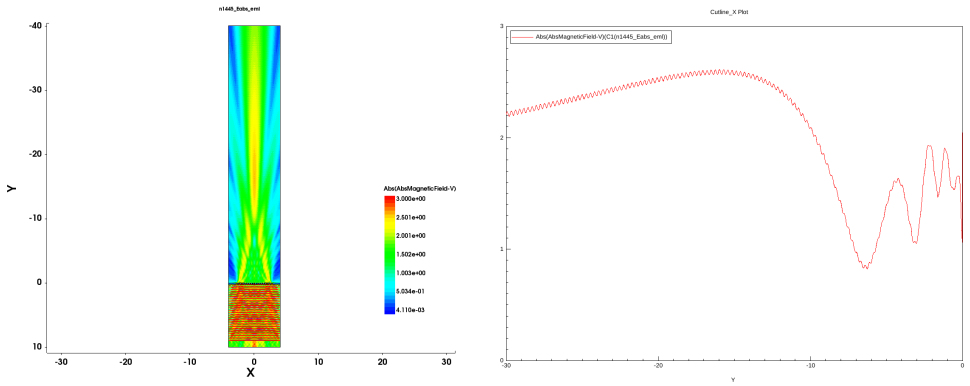

Figure C-32. Results for 400nm gold thickness, 15nm increment,and 17 slits with SiO_2 top and SiO_2 bottom at 800 nm

Bibliography

1. B. Salah and M. Teich, *Fundamentals of Photonics*, 2nd ed. John Wiley and Sons, 2007.

2. A. Rogalski, "History of infrared detectors," *Opto-Electronics Review*, vol. 20, no. 3, pp. 279–308, 2012.

3. M. A. Kinch, *Fundamentals of infrared detector materials.* SPIE Press, 2007, vol. 76.

4. L. D. Wellems, D. Huang, T. A. Leskova, and A. A. Maradudin, "Nanogroove array on thin metallic film as planar lens with tunable focusing," *Physics Letters, Section A: General, Atomic and Solid State Physics*, vol. 376, no. 3, pp. 216–220, 2012.

5. L. Verslegers, P. B. Catrysse, Z. Yu, J. S. White, E. S. Barnard, M. L. Brongersma, and S. Fan, "Planar lenses based on nanoscale slit arrays in a metallic film," *Nano Letters*, vol. 9, no. 1, pp. 235–238, 2009.

6. D. Z.-Y. Ting, C. J. Hill, A. Soibel, S. A. Keo, J. M. Mumolo, J. Nguyen, and S. D. Gunapala, "A high-performance long wavelength superlattice complementary barrier infrared detector," *Applied Physics Letters*, vol. 95, no. 2, p. 023508, 2009.

7. D. Z.-Y. Ting, A. Soibel, L. Hoglund, J. Nguyen, C. J. Hill, A. Khosahkhlagh, and S. D. Gunapala, "Type-II Superlattice Infrared Detectors," in *Advances in Infrared Photodetectors*, 2011, pp. 1–50.

8. L. D. Wellems, D. Huang, T. A. Leskova, and A. A. Maradudin, "Optical spectrum and electromagnetic-field distribution at double-groove metallic surface gratings," *Journal of Applied Physics*, vol. 106, no. 5, 2009.

9. Y. Zhao, S.-C. S. Lin, A. A. Nawaz, B. Kiraly, Q. Hao, Y. Liu, and T. J. Huang, "Beam bending via plasmonic lenses." *Optics express*, vol. 18, no. 22, pp. 23 458–23 465, 2010.

10. H. Shi, C. Du, and X. Luo, "Focal length modulation based on a metallic slit surrounded with grooves in curved depths," *Applied Physics Letters*, vol. 91, no. 9, pp. 23–25, 2007.

11. H. F. Ghaemi, T. Thio, D. E. Grupp, T. W. Ebbesen, and H. J. Lezec, "Surface plasmons enhance optical transmission through subwavelength holes," *Physical Review B*, vol. 58, no. 11, pp. 6779–6782, 1998. [Online]. Available: https://link.aps.org/doi/10.1103/PhysRevB.58.6779

12. M. D. Huntington, L. J. Lauhon, and T. W. Odom, "Subwavelength lattice optics by evolutionary design," *Nano Letters*, vol. 14, no. 12, pp. 7195–7200, 2014.

13. A. D. Rakic, A. B. Djurišic, J. M. Elazar, and M. L. Majewski, "Optical Properties of Metallic Films for Vertical-Cavity Optoelectronic Devices," *Appl. Opt.*, vol. 37, no. 22, pp. 5271–5283, 1998. [Online]. Available: http://www.ncbi.nlm.nih.gov/pubmed/18286006{\%}5Cnhttp://ao.osa.org/abstract.cfm?URI=ao-37-22-5271

14. R. Qiang, R. L. Chen, and J. Chen, "Modeling electrical properties of gold films at infrared frequency using FDTD method," *International Journal of Infrared and Millimeter Waves*, vol. 25, no. 8, pp. 1263–1270, 2004.

15. S. Lal, S. Link, and N. J. Halas, "Nano-optics from sensing to waveguiding," *Nature Photonics*, vol. 1, no. 11, pp. 641–648, 2007.

16. K. F. Warnick, *Numerical Methods for Egineering*. Scitech Publishing, 2011.

17. B. Baumeier, T. A. Leskova, and A. A. Maradudin, "Transmission of light through a thin metal film with periodically and randomly corrugated surfaces," *Journal of Optics A: Pure and Applied Optics*, vol. 8, no. 4, pp. 191–207, 2006.

Vita

Captain Patrick Kennedy received his bachelors degree in electrical engineering from the University of New Hampshire in 2013.

REPORT DOCUMENTATION PAGE

Form Approved
OMB No. 0704–0188

1. REPORT DATE *(DD–MM–YYYY)*	2. REPORT TYPE	3. DATES COVERED *(From — To)*
22–03–2018	Masters Thesis	Sept 2016 — Mar 2018

4. TITLE AND SUBTITLE

Plasmonic Grating Geometries and Wavelength-Dependent Focus Depth in Infrared Detectors

5a. CONTRACT NUMBER

5b. GRANT NUMBER

5c. PROGRAM ELEMENT NUMBER

6. AUTHOR(S)

Kennedy, Patrick, R, Capt, USAF

5d. PROJECT NUMBER

JON 17G334H-FY17

5e. TASK NUMBER

5f. WORK UNIT NUMBER

7. PERFORMING ORGANIZATION NAME(S) AND ADDRESS(ES)

Air Force Institute of Technology
Graduate School of Engineering and Management (AFIT/EN)
2950 Hobson Way
WPAFB OH 45433-7765

8. PERFORMING ORGANIZATION REPORT NUMBER

AFIT-ENG-MS-18-M-038

9. SPONSORING / MONITORING AGENCY NAME(S) AND ADDRESS(ES)

Air Force Research Laboratory Space Vehicles Directorate
Communications and Sensors Section
Dr. Vincent Cowan
3550 Aberdeen Ave Kirtland AFB 87114
(505) 853-4591

10. SPONSOR/MONITOR'S ACRONYM(S)

AFRL/RVSWS

11. SPONSOR/MONITOR'S REPORT NUMBER(S)

12. DISTRIBUTION / AVAILABILITY STATEMENT

DISTRIBUTION STATEMENT A. APPROVED FOR PUBLIC RELEASE; DISTRIBUTION IS UNLIMITED.

13. SUPPLEMENTARY NOTES

This material is declared the work of U.S. Government and is not subject to copyright protection in the United States.

14. ABSTRACT

The objective for this research is to determine a relationship between plasmonic grating geometries and the wavelength-dependent focus depth. This research is focused on enhancing the signal collected by infrared detectors by using a metal grating as a planar lens to focus light in the detecting region of the substrate. This can be used to maintain a thinner absorbing region and possibly to create multi-color imaging in a single pixel. Simulations demonstrate that the plasmonic lens is capable of creating a wavelength dependent focus spot.

15. SUBJECT TERMS

Plasmonics, Plasmonic Gratings, Infrared, Photodetection

16. SECURITY CLASSIFICATION OF:			17. LIMITATION OF ABSTRACT	18. NUMBER OF PAGES	19a. NAME OF RESPONSIBLE PERSON
a. REPORT	b. ABSTRACT	c. THIS PAGE			Maj Tod Laurvick
U	U	U	U	78	19b. TELEPHONE NUMBER *(include area code)* (937) 255-3636 x4382 tod.laurvick@afit.edu